Interpretation of run-of-mine comminution and recovery parameters using multi-element geochemical data clustering

van Duijvenbode, Jeroen R.; Cloete, Louis M. ; Shishvan, Masoud S.; Buxton, Mike W.N.

DOI
10.1016/j.mineng.2022.107612

Publication date
2022

Document Version
Final published version

Published in
Minerals Engineering

Minerals Engineering 184 (2022) 107612

Contents lists available at ScienceDirect

Minerals Engineering

journal homepage: www.elsevier.com/locate/mineng

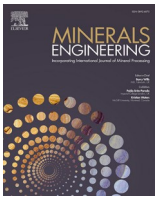

Interpretation of run-of-mine comminution and recovery parameters using multi-element geochemical data clustering

Jeroen R. van Duijvenbode [a,*], Louis M. Cloete [b], Masoud S. Shishvan [a], Mike W.N. Buxton [a]

[a] Resource Engineering Section, Department of Geosciences and Engineering, Delft University of Technology, Stevinweg 1, 2628 CN Delft, the Netherlands
[b] AngloGold Ashanti, Johannesburg, South Africa

ARTICLE INFO

Keywords:
Tropicana Gold Mine
Agglomerative hierarchical clustering
Mineral processing
Mining
Geochemistry
Four-acid digestive multi-element ICP data
Comminution and recovery parameters

ABSTRACT

Multi-element (ME) datasets provide comprehensive geochemical signatures of an orebody and are commonly used to gain insight into the mineralogy, lithology, alteration patterns and to identify target-pathfinders. However, little effort is made in using these data to explain comminution or recovery characteristics. This paper describes an agglomerative hierarchical clustering approach applied to ME data from the Tropicana Gold Mine, Australia, and investigates the relationship between the resultant classes and run-of-mine comminution and recovery parameters. First, it is demonstrated how an industry scale ME dataset is prepared for clustering. The preparation consists of verifying the absence of interlaboratory and intralaboratory bias between measurements, centred log-ratio transformation (clr), normalisation and principal component analysis (PCA). Afterwards, the first case study indicate that the clustering separation is primarily driven by geochemical differences caused by major rock-forming mineral signatures (felsic vs mafic, alteration vs no alteration, chert or quartz lithologies, unmineralised vs mineralised material). This case study separates the ME dataset into five unmineralised and two Au-mineralised material classes. The second case study continues with the two identified mineralised material classes and further separates these samples into five new classes. These classes are explored geochemically and by using the spatial context (within domains) better matched with metallurgical test results. It is found that domain-related material class proportions assist in interpreting different processing proxies such as the Equotip hardness (Leeb), Bond Work index (BWi), Axb, and processing recovery and reagent consumption. Knowledge of the processing parameters per domain and class composition can be used to infer such characteristics in the absence of standard metallurgical tests. This new approach of gaining insights into comminution and recovery parameters through geochemical analysis demonstrates the benefit of the conceptualised material fingerprinting concept.

1. Introduction

Multi-element (ME) geochemical datasets (four-acid digestion) are among the most quantitative and informative information a mining company can collect. Together with the geological, mineralogical, and geophysical data, it forms the core datasets that describe different material attributes. Geochemical or ME data provide quantitative results that are chiefly used to identify mineralisation and gage exploration potential. For example, various studies have used this proxy relationship for mineral exploration potential (CSA Global Canada Geoscience Ltd, 2018; Gazley et al., 2015; Grunsky and de Caritat, 2019; Zhou et al., 2017), automated geological logging (Hill et al., 2020), or mapping mineralisation signatures and magmatic and hydrothermal processes (Brauhart, 2019; Escolme et al., 2019; Gaillard et al., 2018; Halley, 2020; Motoki et al., 2015).

A common outcome from the studies mentioned above is that the mineralisation and alteration processes result in zones or domains with distinct geochemical characteristics. These geochemical domains then reflect the mineralogy, which sometimes may be difficult to recognise using geological mapping or logging practises, e.g., in domains with overprinting alteration events or metasomatism (Caciagli, 2016). Sequentially, the geochemical and mineralogical domains can support a more concrete link with metallurgical variables such as comminution properties (hardness, grindability), metal recoveries or reagent consumption (Caciagli, 2016). Commonly, these relationships are only inferred from extensive small-scale metallurgical tests, such as breakage,

* Corresponding author.
E-mail address: j.r.vanduijvenbode@tudelft.nl (J.R. van Duijvenbode).

https://doi.org/10.1016/j.mineng.2022.107612
Received 26 November 2021; Received in revised form 26 April 2022; Accepted 1 May 2022
Available online 23 May 2022

liberation, and abrasiveness, as described by Wikedzi et al. (2018) and Lynch (2015), modelled using simulation (Madenova and Madani, 2021), or focus only on the Bond Work Index (Bhuiyan et al., 2019). However, published studies that consider the relationships of ME-based material classes with both comminution (processing) characteristics and recovery potential are lacking. The purpose of this paper is to address this gap. The following paragraphs discuss practices in merging mining related datasets to prepare the ME and metallurgical datasets for analysis.

Geochemical datasets are typically challenging to interpret because they are collected across multiple years and using different laboratories, analytical tools and methods. Therefore, careful analysis needs to be done to interpret the multi-dimensional data effectively (Grunsky and de Caritat, 2019). The current study shows the efforts undertaken to ensure a reliable dataset could be used for further analysis. Such efforts include adequate levelling of multiple datasets and detection of missing values. Furthermore, ME data are compositional and require transformation to log-ratio coordinates to account for closure (Aitchison, 1999; Grunsky and de Caritat, 2019; Pereira et al., 2016).

There is a second problem in using existing datasets from mining companies. Historical data collection typically does not conform to an ideal tiered geometallurgical data structure, as presented in Fig. 1 (Dominy et al., 2018; Keeney, 2010). The problem is that Level 1, or geometallurgical proxy data, typically does not provide a direct measure of metallurgical response. However, via correlations, it can be used to infer metallurgical characteristics. In contrast, historical Level 3 and 4 data (representing most metallurgical tests) are commonly not co-located to lower-order data types, and insufficient effort is made to establish direct correlations to Level 1 or Level 2 data types. The establishment of these correlations is desired because more densely spaced proxy or support data provides a more representative view of ore variability, observed across and within domains, which in turn drives inherent metallurgical characteristics that may ultimately manifest as process response variability. A further, often underappreciated, benefit of employing the ideal tiered geometallurgical data structure is that it allows one to proactively domain the deposit of interest and align subsequent metallurgical sampling to the resulting domains, thereby ensuring more effective coverage, which is especially important when dealing with the allocation of sparse higher-order tests.

This research will propose a way to retrospectively stitch ME proxy data and metallurgical test data together using geochemical data clustering, mineralogical interpretations, and considerations of spatial domains, addressing the existing lack of co-located datasets. Co-location is typically limited due to the infrequency of metallurgical test campaigns relative to gold assays and ME analysis, which is typically collected on every meter of drill core or chips. In metallurgical testing, the entire core length spanning the zone is typically used as a single composite, which effectively smooths the result and may underrepresent the overall variability of the response. Typically, the issue of non-collocation can still be overcome by ME analysis of sample splits from the larger metallurgical sample. These can then be used, in conjunction, to infer processing properties.

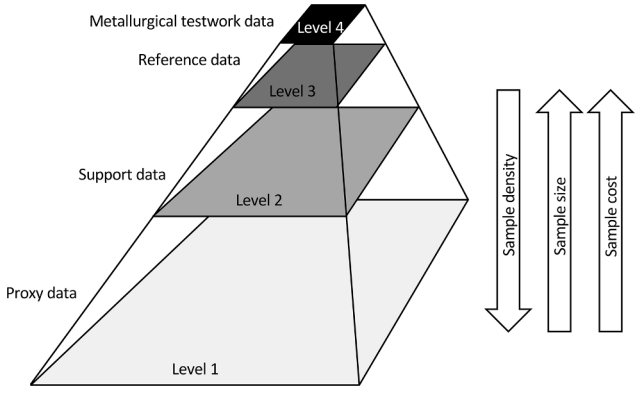

Fig. 1. Tiered geometallurgical data types (modified after Dominy et al. (2018) and Keeney (2010)).

Despite these limitations, combinations of these data with more widely available proxy datasets such as drilling penetration rates and Equotip hardness data provide a broader view of the material classes. Then, even a small dataset becomes very useful and can be used to determine the processing attributes of different material types. Additionally, it is advisable to utilise basic (proxy) datasets to drive metallurgical sample selection rather than blindly compositing and sampling to fulfil test mass requirements, see for example, the sampling dilemma described by Lamberg (2011). For these reasons, a better interpretation approach of the comminution and recovery characteristics is needed based primarily upon the ME (and other proxy) data.

To interpret varying comminution or recovery characteristics, one should successfully fingerprint material from different geological domains that reflect changes in mineralogy, rock texture and rock competency. In this context, a fingerprint is a material classification based on the similarity of the measured and constitutive material attributes (van Duijvenbode et al., 2020). As a first step to construct fingerprints, one could consider clustering elemental concentrations. Clustering is a method to partition samples with similar characteristics (Romary et al., 2015). In the case of ME data clustering, this results in a geochemical signature and may correlate to a specific suite of minerals, but also with physical properties such as grain size, texture, hardness, or brittleness of the related material. For example, Hunt and Berry (2017) show the correlation between Point load index and Equotip across different deposit styles. Although the current study focuses on using geochemical data, material fingerprints should ideally also be constructed using a multivariate combination of mineralogical, geophysical and geomechanical data as these constitutive attributes can easily be added to the fingerprints during clustering. In general, this process can be considered an addition, refinement or validation of the clustering classes. The remainder of this section discusses the structure of the paper.

This paper presents an unsupervised clustering approach of ME data and investigates the relationship between the resulting classes and comminution and recovery parameters. Clustering is done for two case studies from the Tropicana Gold Mine, Western Australia, which show one clustering exercise each. Case Study I is focused on finding geochemical signatures related to (predominantly) gold mineralisation. In comparison, Case Study II focuses on unravelling the root cause of observed processing behaviour for the different mineralisation styles. This is done based upon re-clustering the Au-mineralised classes defined in Case Study I. This relationship between mineralisation and comminution behaviour is explained by exploring each class's geochemical signature and then linking them with legacy metallurgical test results across the different classes and spatial domains. The contribution is to provide tools to extract value from industrial-scale geochemical datasets and quantify material classes in terms of processing parameters. First, the data pre-processing steps are explained. This may help other researchers to extract similar values out of raw datasets. Second, we show the dimension reduction and clustering approach. Third, the geochemical signatures of the clustering classes are explored and illustrated how these relate to typical comminution and recovery parameters.

2. Geology of the Tropicana Gold Mine

Samples for this study were obtained from the Tropicana Gold Mine (TGM), which is located along the south-eastern margin of the Yilgarn craton in the Albany-Fraser Orogen, Western Australia (Fig. 2). The deposit is hosted in Archaean amphibolite-granulite facies metamorphic rocks. The banded, gneissic host rocks range from mafic to felsic, although most are broadly intermediate compositions (Crawford and Doyle, 2016). The mineralised zones are hosted within a sequence of high grade quartzofeldspathic and garnet-bearing gneisses, with

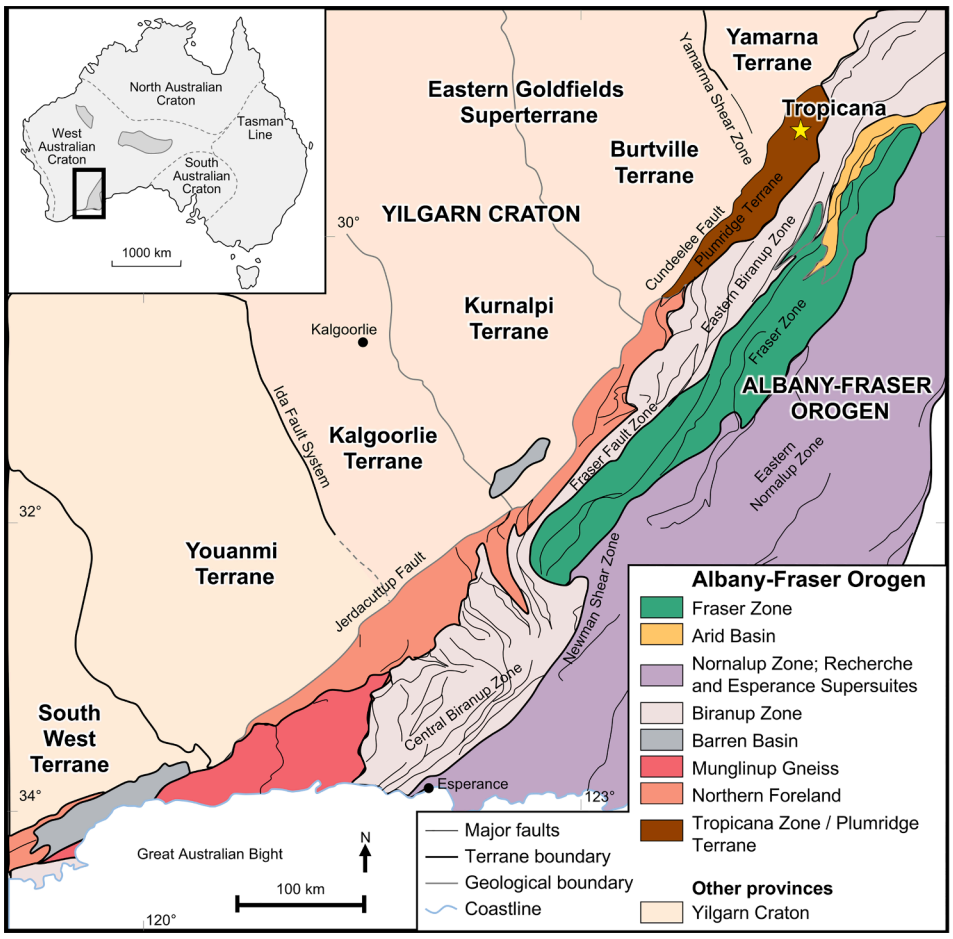

Fig. 2. Regional geological map of the Albany-Fraser Orogen with respect to the eastern margin of the Yilgarn Craton, Western Australia, showing the location of the Tropicana gold deposit. Modified after Spaggiari et al. (2011).

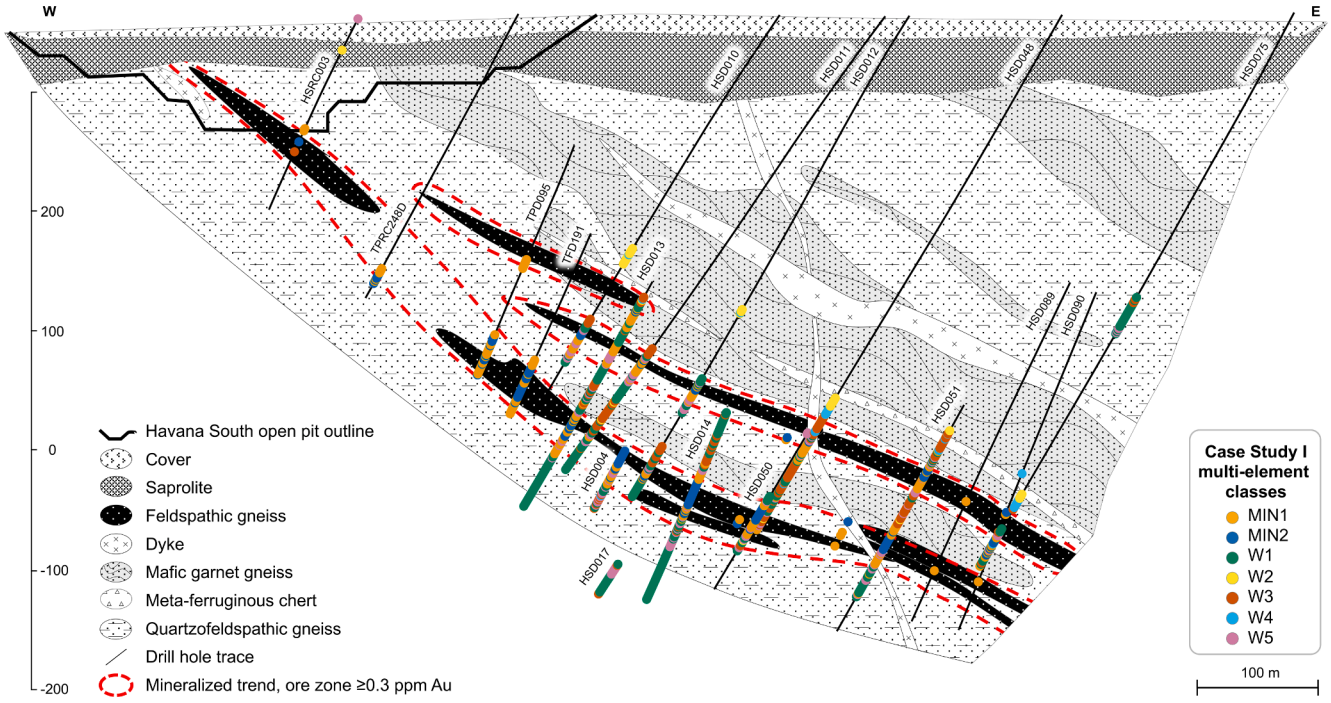

Fig. 3. Schematic EW cross-section of the Havana South domain showing the deposit geology (100 m thick at 649753 mE, 6761137 mN, azimuth 37°, GDA/UTM grid). The superimposed ME class labels from Case Study I samples are discussed in Section 5.1.

amphibolites, granulites, metasedimentary cherts, and pegmatites (Fig. 3). This figure is an illustrative cross-section of the Havana South domain showing the geometry and style of mineralisation. Similar geometries are exhibited in the other deposits. Post mineralisation faulting resulted in four main distinct structural domains, which are from north to south, including the sample proportions from each: Boston Shaker (23.9%), Tropicana (39.3%), Havana (including Havana Deeps, 10.2%) and Havana South (26.6%). The mine's historic cut-off grade was at $\geq$ 0.3 ppm Au.

The mineralised zones occur as one or two laterally extensive planar lenses with a moderate dip. The favourable host to mineralisation is a deformed feldspathic gneiss dominated by perthitic K-feldspar. Within the mineralised zone, biotite, sericite, and pyrite alteration replaced the metamorphic mafic minerals and feldspar (Blenkinsop and Doyle, 2014; Crawford and Doyle, 2016; Hardwick, 2021). Perthitic K-feldspar rich end-members have a higher K/Al (molar) ratio than the plagioclase-rich end-members. Hardwick (2021) discriminated that these higher K/Al molar ratios of the feldspathic gneiss units are more controlled by higher modal proportions of perthitic K-feldspar with partial melting textures rather than by enrichment in biotite (since higher K/Al (molar) trends towards the K-feldspar node on an Al-K-Mg molar ternary plot). Relative to the unmineralised host rocks, the mineralised rock exhibits significant enrichment in S and the ore elements (Mo, Te, Tl, Ag, Au, W) and K-group elements (K, Rb, Hf, Zr, U) (Crawford and Doyle, 2016).

3. Methods

3.1. Data acquisition and pre-processing

This study focuses on 30,687 ME samples from the Tropicana Gold Mine area collected until June 2019. These samples have been routinely collected during exploration and were predominantly taken over one-meter intervals from NQ2 diamond core (core approx. 75.7 mm in diameter) across the orebody and adjacent unmineralised envelope (up to 18 m) in the hanging wall and footwall of the deposit. The samples were analysed in four different laboratories by four-acid digestion, which is a technique that effectively decomposes almost all rock-forming minerals (Grunsky and de Caritat, 2019). The resulting acid solution was then analysed by inductively coupled plasma optical emission spectrometry (ICP-OES) or inductively coupled plasma mass spectrometry (ICP-MS). The final results contain elemental concentrations for 48 elements. In addition, the samples were also assayed for gold (Au) concentration using (primarily) a 50 g charge fire-assay analysed by solvent extraction Atomic Absorption Spectroscopy (AAS) or MS. This dataset with samples and elemental concentrations was further filtered and prepared by the following three steps:

1. Element availability: The objective was to indicate for all samples whether the measured element must be considered for further clustering or not. Only elements that were measured in>95% of the samples were considered. This mostly represents the suite of common elements analysed in commercial four acid digest packages. Any additional element (Re, Ge, Eu) added would reduce the potential number of samples by at least 15%. The analysed (44) elements are Ag, Al, As, Ba, Be, Bi, Ca, Cd, Co, Cr, Cs, Cu, Fe, Ga, Hf, In, K, Li, Mg, Mn, Mo, Na, Nb, Ni, P, Pb, Rb, S, Sb, Sc, Se, Sn, Sr, Ta, Te, Th, Ti, Tl, U, V, W, Y, Zn and Zr. The Au concentration is also known for most samples but not further considered during clustering. Excluding Au from clustering guarantees that the resulting class signatures focus on major and other trace elements, describing the geochemical environment where Au may be found.

If, for a specific element, the proportion of values less than the analytical detection limit is too high, then an element value becomes a boolean indicator addressing whether an element is present or absent in a sample. There are two issues with these elemental concentrations in preparing them for clr representation. Firstly, if they are considered for closure, they will most likely distort the actual values of other elements since the real elemental concentration is unknown. Secondly, if this element is ignored in its entirety, we also neglect the important information that the element is present in some samples.

Various imputation techniques for below detection or missing data exist, including a simple substitution, lognormal replacement or multivariate expectation maximisation algorithms (Palarea-Albaladejo et al., 2014). In the dataset, As, Bi, Sb and Te were censored in about 60% of the samples and Se was censored in 93.5% of the samples. Martín-Fernández et al. (2012) recommend excluding elements with > 30% of values below detection limit, which was done for Se, but not for As, Bi, Sb, and Te. After testing with the inclusion or removal of these elements, it was found that limited differences were found in the clustering results. Therefore, it was preferred to keep these elements, as especially As and Te are important trace elements in an orogenic Au deposit. Note that during Case Study II, this percentage of values below detection limit dropped below 30%. All elemental values below detection limit were simply substituted with values half of the detection limit (Carranza, 2011; Grunsky and Smee, 1999).

2. Dataset quality: The data are acquired across multiple years (2003–2019), four different laboratories, and with different analysis methods. Therefore, the quality of the geochemical data was checked and confirmed using 1,053 certified reference material (CRM) measurements representing the two largest laboratories. The other two laboratories are used infrequently and, due to the small sample representation (accountable for 1% of the samples), assumed to have no major influence on the precision or bias of the dataset. In 95% of the batches, at least one of the following seven CRMs were used consistently: AMIS0167, OREAS 24b, OREAS 25a, OREAS 45d, OREAS 45e, OREAS 502b or OREAS 520. The expected concentration of each element and its variation range (at two standard deviations) are known for these standards. Based on these known values, the interlaboratory (reproducibility) and intralaboratory (repeatability) data quality is checked. If all conditions are satisfied, then the data are considered high enough quality, and no additional data filtering is required. When differences in the precision of samples or elements are noticed, individual batch samples or elements can be discarded.

The three quality metrics used are precision, bias and Horwitz Ratio (HorRat). The precision indicates the deviation from the best value (BV) expressed as the percent relative standard deviation (RSD%) of the CRM values. The accuracy is reported as bias which is calculated as the percent difference between the average CRM value obtained from the laboratory measurements and the best value (BV) recommended by the CRM certificate (Ordóñez-Calderón et al., 2017). The HorRat is a metric that quantifies the measurement performance with respect to precision (Horwitz and Albert, 2006) and is calculated (for single-laboratory validation) as follows:

$$HorRat_r = \frac{observedrelativeSD}{predictedrelativeSD} = \frac{RSD_r}{PRSD_R}, \quad (1)$$

where $PRSD_R$ the predicted reproducibility obtained from the Horwitz equation and calculated as $PRSD_R = 2^{*}\left(certified\,value_{CRM}{*}10^{-6}\,(ppm\,to\,concentration)\right)^{-0.15}$, and subscript r and R indicating the repeatability (intralaboratory) and reproducibility (interlaboratory) conditions, respectively. This equation transforms the RSD% found to a fraction of the RSD% expected and equals to 1 for exact correspondence. The precision is better than expected if the HorRat is <1, and poorer if >1. Under reproducibility conditions, the empirically acceptable range is from 0.5 to 2.0 and under repeatability conditions between 0.3 and 1.3 (Horwitz and Albert, 2006; Rivera et al., 2011).

3. Transformation and normalisation: The ME data used are compositional in nature and have associated problems of closure (Aitchison, 1999). Before samples can be compared, the sample composition will require transformation to log-ratio coordinates with respect to the identified elements. This study uses a centred log-ratio (clr) transformation, which transforms the data coordinates from the

simplex, an *n*-dimensional composition within the positive real number space, to the Euclidean real space, which is more suitable for statistical analysis (Aitchison, 1986; Bhuiyan et al., 2019).

3.2. Clustering

This study used agglomerative hierarchical clustering to partition the samples into clusters (Wierzchoń and Kłopotek, 2018). The clustering method is iterative and starts with each sample in its own cluster. Then, the algorithm calculates the distance for each cluster pair (Euclidean distance matrix) and finds the closest pair. The metric to calculate the distance can differ, and the present study uses Ward's method. This minimises the sum of squares of distances between samples and the cluster centres to which the samples belong. The two selected clusters are merged into a new cluster. Afterwards, the distance matrix is updated by calculating the new distance from the new cluster to all other clusters. These merge and update steps are repeated until only one single cluster is formed (Wierzchoń and Kłopotek, 2018). The final number of clusters is selected based upon the silhouette score, Calinski-Harabasz index and Davies-Bouldin index. All these metrics are internal clustering validation measures and are used to determine the optimal number of clusters (Aggarwal and Reddy, 2014). The final number agreed upon across the methods is used for the final clustering exercise. The number of clusters is dependent on the set of input samples.

4. Quality assurance and quality control

4.1. Precision, bias and HorRat

Table 1 summarises the analytical results for OREAS 45d and a few selected elements described in this study. The results for all other CRMs and elements are provided in Supplementary Materials Table A.1. The CRM analysis indicates precision better than 10% for most major and trace elements, and 10 to 15% for Ag, In and Zn. The bias is better than ± 10% for most elements in both laboratories. Laboratory 2 has a bias of 35% for Ag and −11.7% for Cr. The same precision and bias conclusions are generally valid for all other CRMs and elements (Supplementary Materials Table A.1). The intralaboratory $HorRat_r$ ratios obtained for most elements were within the acceptable range of 0.3–1.3 under repeatability conditions (Table 1). However, laboratory 2 has suspect $HorRat_r$ values for various oxide bearing elements (e.g., Al, Ca, Fe) measured with OES, while the precision and bias are within 10%. Several possible causes emerge from the analysis of HorRat values displayed in Fig. 4.

Fig. 4a and Fig. 4b contain the intralaboratory $HorRat_r$ values for laboratories 1 and 2, respectively. A darker red square indicates higher HorRat values (>1.3) than expected and can be explained by three causes. First, a few outliers cause the RSD% to increase too much (outliers above BV: Ca, Mn, Na, Pb, Zn, Zr; outliers below BV: Cr, Fe, K, S, Ti). Removing these outliers would decrease the HorRat value within the acceptable ranges. Second, there is a relatively larger bias in the measurements either below (As) or above (Sb) the BV. This is often in conjunction with the BV being close to the LDL (Pb, Sc), resulting in less precise measurements. However, this is not indicated as a problem because other CRMs are better to assure the precision and bias of these elements in the dataset. Third, a large group of the elements (Al, Ca, Fe, P, S, Ti, Zn) measured with ICP-OES in laboratory 2 have precision and bias better than ± 10% (Supplementary Material Table 1), but $HorRat_r$ close to or above 1.3. For most of these elements, the SD is smaller than expected from this CRM, indicating that the laboratory measurements are better than anticipated. A dark blue square indicates lower HorRat values (<0.3) than expected and links to the following cause. There is a large group of elemental concentrations (Bi, Cs, Th, Tl, U) within ± 1 SD. This means that there is a higher RSD% as anticipated from the CRM. Finally, a white square indicates that no proper data were available because the measurement technique cannot measure the specific element or the CRMs elemental concentration is in>50% of the measurements below the detection limit. This, for example, is the case with Cd and Te of OREAS 45d.

The interlaboratory $HorRat_R$ values are represented in Fig. 4c and indicate how laboratories 1 and 2 perform compared. The shown $HorRat_R$ values are the mean of the $HorRat_r$ values presented in Fig. 4a and Fig. 4b. In laboratory 1, there are a few elements (Co, Cs, Ga, Mo, Tl) with $HorRat_R$ values much lower than the acceptable lower limit of 0.5. Laboratory 2 has slightly higher HorRat values for most oxide elements. As indicated above, the precision and bias for these elements are still good.

Additionally, there are a few large outlier measurements that were not removed prior to analysis, for example, Al. Also, note that an elevated Al concentration can indicate that the digestion was not taken to incipient dryness and causes the Al to remain in the test tube as an insoluble fluoride complex. Outliers were not removed because the large dataset and applied transformations would reduce their effect. Overall, the Al (and the other oxides) HorRat values for laboratory 2 are impropriate, but its precision (7.2%) and bias (2.3%) are good. Since the $HorRat_R$ values of most of the elements are within the acceptable ranges

Table 1
Analytical data for intralaboratory measurements of OREAS 45d for laboratories 1 and 2. Precision is expressed as percent relative standard deviation (RSD%). Bias is calculated as the percent difference between the average and the best value (BV) of the OREAS 45d certificate. The lower detection limits (LDL) are reported for the analytes and analysis method used by the laboratory. The entire table, including the remaining elements and CRMs, can be found in Supplementary Material Table A.1.

Elem.	Analysis	Unit	BV	Laboratory 1						Laboratory 2					
	method			LDL	Avg.	SD	RSD(%)	Bias(%)	$HorRat_r$	LDL	Avg.	SD	RSD(%)	Bias(%)	$HorRat_r$
Ag	MS	ppm	0.2	0.1	BV is too close to the LDL value					0.05	0.27	0.04	14.8	35	0.7
As	MS	ppm	13.8	2	13.9	0.52	3.7	0.5	0.3	1	13.4	1.17	8.7	−2.7	0.8
Bi	MS	ppm	0.31	0.05	0.32	0.02	6.2	3.2	0.3	0.1	0.3	0.02	6.7	−3.2	0.4
In	MS	ppm	0.1	0.05	0.09	0.01	11.1	−10	0.5	0.02	0.09	0.01	11.1	−10	0.5
Mo	MS	ppm	2.5	0.1	2.49	0.1	4	−0.4	0.3	0.1	2.65	0.15	5.7	6	0.4
Rb	MS	ppm	42.1	0.1	42.3	1.32	3.1	0.5	0.3	0.05	43.7	2.22	5.1	3.8	0.6
Sr	MS	ppm	31.3	0.5	32.1	1.39	4.3	2.6	0.5	0.1	32.7	1.83	5.6	4.2	0.6
Th	MS	ppm	14.5	0.05	14.4	0.34	2.4	−0.6	0.2	0.05	14.8	0.96	6.5	2.1	0.6
U	MS	ppm	2.63	0.05	2.62	0.11	4.2	−0.4	0.3	0.05	2.67	0.18	6.7	1.5	0.5
Al	OES	%	8.15	0.005	8.09	0.19	2.3	−0.7	0.8	0.01	7.91	0.6	7.9	−3	2.7
Ca	OES	ppm	1854	50	1918	110	5.8	3.5	1.1	50	1924	136	7.0	3.8	1.4
Cr	OES	ppm	549	1	549	29.3	5.3	0.1	0.9	10	484	26.6	5.5	−11.7	0.9
Fe	OES	%	14.51	0.01	14.5	0.32	2.2	−0.3	0.8	0.01	14.12	0.61	4.3	−2.7	1.6
K	OES	ppm	4123	20	4227	129	3.1	2.5	0.7	100	4072	184	4.5	−1.2	1.0
Mg	OES	ppm	2447	20	2404	83.9	3.5	−1.7	0.7	20	2378	110	4.6	−2.8	0.9
Na	OES	ppm	1006	20	1003	46.5	4.6	−0.3	0.8	50	980	48.4	4.9	−2.6	0.9
S	OES	ppm	486	50	486	20.7	4.3	−0.1	0.7	20	482	31.4	6.5	−0.8	1
Zn	OES	ppm	45.7	1	44.1	4.13	9.4	−3.6	1	5	45.8	4.93	10.8	0.2	1.2

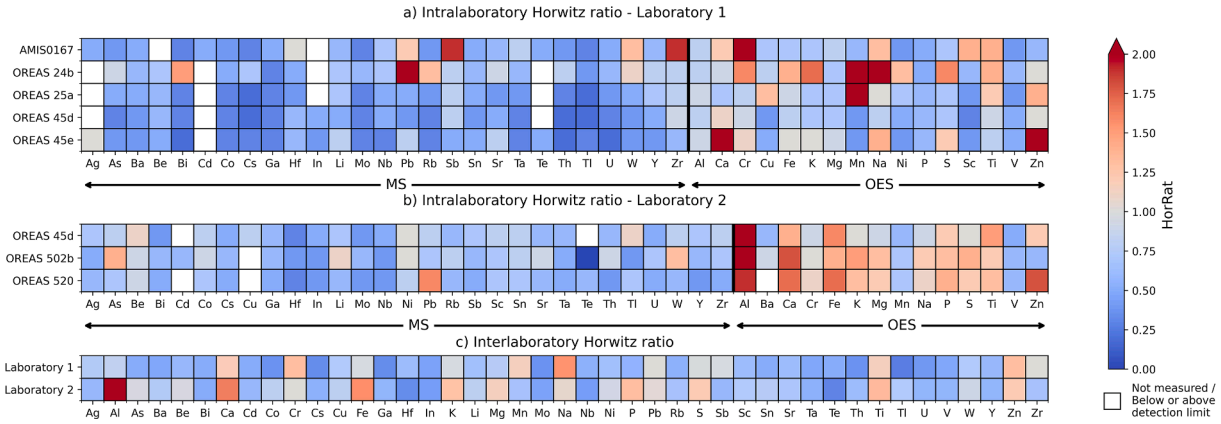

Fig. 4. Intralaboratory (a and b) and interlaboratory (c) Horwitz ratio overview of certified reference material (CRM) – element pairs measured in two laboratories. The empirical accepted intralaboratory Horwitz ratio range is between 0.3 and 1.3, and the interlaboratory Horwitz ratio range is between 0.5 and 2.0.

(0.5–2.0), it can be concluded that the four-acid digestion measurements of the different laboratories can be compared.

4.2. Summary of data reduction constraints

In summary, it is observed that there is a difference in precision for certain elements. For most oxide bearing elements, such as Al, Ca, K, Mn, Na, S and Ti, there is a small overestimation of the concentration (average RSD% is 5.5%, bias is + 2.3%). The majority of the other elements are of good quality and may experience underestimation rather than overestimation. As a result, this reduces the tendency for over-optimistic conclusions. Most of the values can be improved by simply removing a single outlier. This means that the batch measurements are reliable and that the different instrumentation methods can be compared. The results from blanks indicate no significant contamination with elements of interest in this study. In addition, the mine's standard quality assurance and quality control procedure for every batch would have highlighted measurement deviations, and the corresponding batches would be re-assayed prior to uploading them to the database. Accordingly, the ME geochemical dataset is deemed of good quality.

Indium, Cd and Se were removed from the original list of elements resulting in 41 elements being considered for clr transformation: Ag, Al, As, Ba, Be, Bi, Ca, Co, Cr, Cs, Cu, Fe, Ga, Hf, K, Li, Mg, Mn, Mo, Na, Nb, Ni, P, Pb, Rb, S, Sb, Sc, Sn, Sr, Te, Ta, Th, Ti, Tl, U, V, W, Y, Zn and Zr. The values of these elements underwent clr transformation and, afterwards, were normalised by a z-score normalisation. The feature dimension of this dataset was reduced using Principal Component Analysis. The number of principal components (PCs) was automatically set to the amount that can describe 95% of the data variance. The lower-dimensional dataset, i.e., the output of the PCA, functioned as the input for clustering.

Several data reduction measures are considered before clustering based upon the precision, bias and HorRat values. These constraints are primarily taken to produce discrete clustering classes not affected by any of the observed elemental concentration deviations. Any following conclusions may consider the excluded elements again, but while taking their flaws into account. The following data constraints are taken:

- Although not obvious from the quality metrics, indium was measured outside the 2 SD range in 31% (average RSD% of 9%) of the CRM measurements and was also in 65% of the samples below the detection limit. Therefore, indium will not be considered during clustering.
- Determining the precision and accuracy of Cd was difficult as it was only possible with two CRMs. The corresponding HorRat was sufficient (~0.6); however, its precision (11.3%) and bias (60%) were considered to be too high and, therefore, Cd will be ignored.
- Most HorRat and z-score acceptable range breaches could be linked to one CRM element outlier. This does not mean that the entire batch was wrong. There was one batch with significant outliers (>4 SD) in 31 elements. The samples corresponding to this batch were not further considered.
- The effect of outliers, in general, is also reduced by the performed clr transformation (this is especially useful for the oxide bearing elements).

4.3. Communition and recovery proxies

A few material hardness proxies were collected at TGM and were selected for review in this study based on availability. These include: the Bond Ball Mill Work index (BWi in kWh/t), the JK rock breakage parameters and expressed as comminution index Axb and Equotip rebound hardness measurements. The BWi determines the relative energy requirements to deliver a specified target particle size (typically either 106 μm or 75 μm) given a certain feed particle size, and and are rock-specific dimensionless parameters determined by fitting a model to the experimental data generated from a drop weight test (Lynch, 2015). Higher values of Axb indicate softer rocks, whereas higher values of BWi indicate harder rocks. The BWi and Axb values are infrequently collected during metallurgical testing campaigns. However, they are direct proxies for processing attributes such as throughput and resulting grind size (Lynch, 2015). Equotip measurements are taken on diamond drill core, aligned to the standard Au assay intervals of one meter. Generally, ten measurements were taken per sample, and for this study, simply the median value was chosen to give one data point per meter. The measurements are frequently collocated with samples used for ME analysis but also include larger portions of the immediate hanging and footwall. The Equotip hardness-testing tool yields Leeb (Ls) values, where a higher Leeb corresponds with a harder sample.

Fig. 5a-c show summary statistics of Equotip, BWi and Axb measurements taken on primarily mineralised material across all deposits. The Leeb values (Fig. 5a) are at the high end of the value range (between 0 and 1000 Leeb), indicating relatively hard rock properties. The mineralised material itself has an expected Leeb value between 750 and 850. Higher values probably relate to increased proportions of quartz, amphibolite and garnet content in the samples. Fig. 5b displays the BWi histogram with a bimodal distribution where one mode is around 16 kWh/t, and the other one is closer to 20 kWh/t. In contrast, the Axb (Fig. 5c) shows a right-skewed distribution with the mode around 38.6. The lower BWi typically resembles samples closer to the surface and is related to either the lower saprolite or transitional ore. The absence of a bimodal signature in the Axb most likely resembles the different test responses on these rock types.

The recovery proxies used in this study are the 48-hour leach

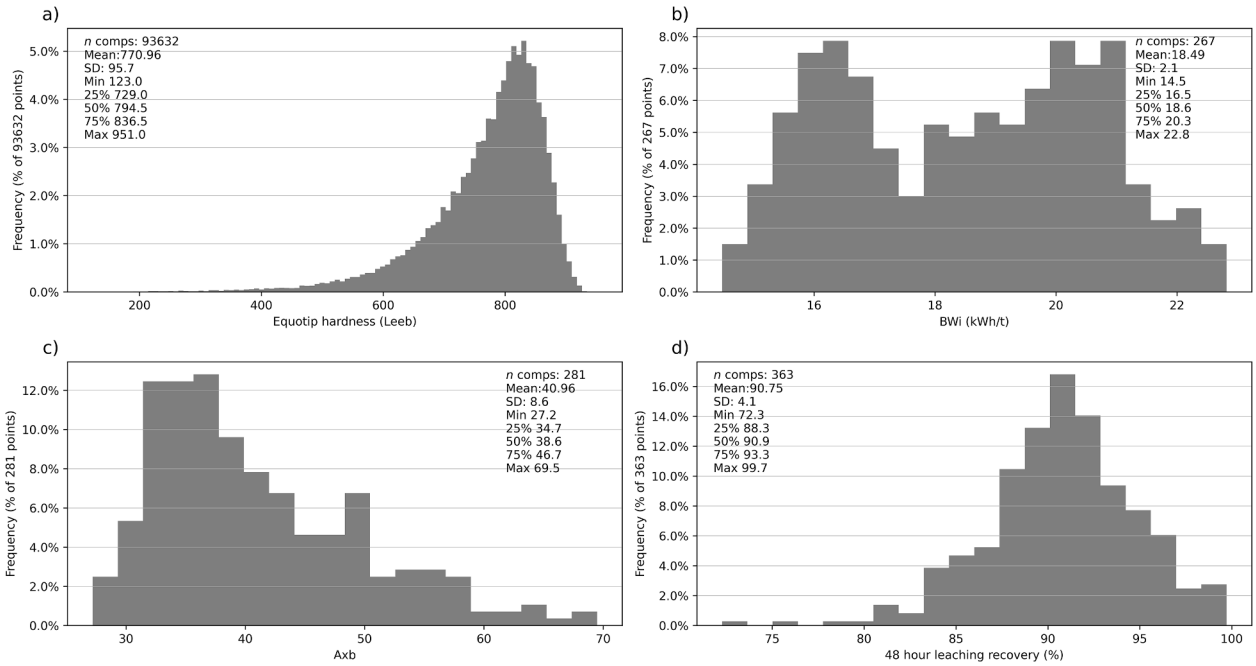

Fig. 5. Summary statistics. Histograms of the Equotip rebound hardness, BWi, Axb and 48-hour leach recovery taken across all geological domains.

recovery (in %), lime consumption (kg/t) and cyanide consumption (kg/t). Fig. 5d shows summary statistics of the recovery values. Among these composites, there is an average recovery of 90.75%. The recovery typically decreases with the depth of the mined material and due to increasing S and Te content (Baker, 2020).

5. Results

5.1. Case Study I: Geochemical mineralised and unmineralised rock separation

5.1.1. Elemental patterns derived from PCA

The 30,687 samples with 41 input features (clr-transformed element values) were reduced to 24 PCs accounting for 95% data variability. Element eigenvectors are plotted in PC1-PC2 and PC2-PC3 space in Fig. 6. A few generalised features are evident from these biplots, which account for 59% of the data variability. Five groups of elements are defined by similar vector orientation and magnitude: (1) with positive PC1 loadings, there are elements generally indicating mafic/ultramafic units, e.g., Ca, Co, Cr, Fe, Mg, Mn, Ni, and Zn; (2) a negative PC1 and positive PC2 relates to elements which are commonly associated with gold mineralisation at TGM (Crawford and Doyle, 2016), e.g., Ag, As, Bi, Mo, S, Te, U, and W; (3) the negative loadings of PC2 identifies elements related to sodic alteration (Be, Na, Sr), and (4) in combination with negative PC3 loading also with elements related to potassic alteration: K, Rb, Ba, Tl, and Cs; (5) elements with a positive PC3 loading relate to the group of relatively immobile elements, e.g., Ta, Nb, Hf, Zr, and Th. These element groupings show similarities to the PCA analysis of the Hamlet orogenic Au deposit in Western Australia (Hood et al., 2019).

The PC features were partitioned into seven clusters (classes) as that number was determined to be optimal based on the mean silhouette score, Calinski-Harabasz index and Davies-Bouldin index (see Supplementary Material Fig. A.1). The Case Study I clustering aims to find a geochemical signature related to mineralisation, where mineralised (≥0.3 ppm Au) and unmineralised (waste) material will be separated. This is the first step in relating processing parameter proxies, as afterwards the primary focus is on mineralised material (Section 5.2).

The PC biplots were further used to investigate early relationships

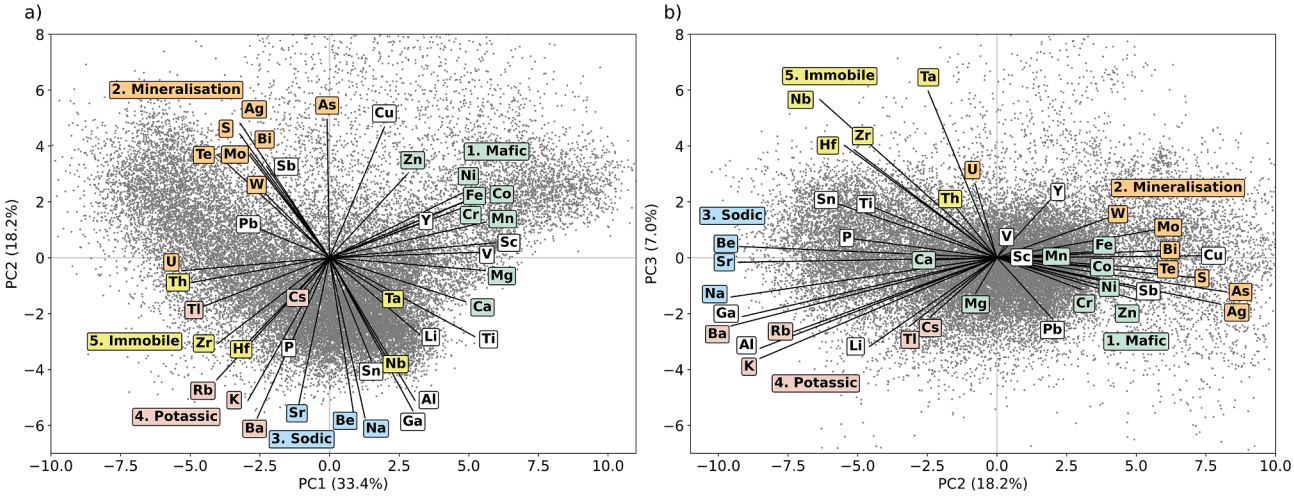

Fig. 6. Principal component biplot of clr-transformed elements plotted on a) PC1-PC2 space and b) PC2-PC3 space.

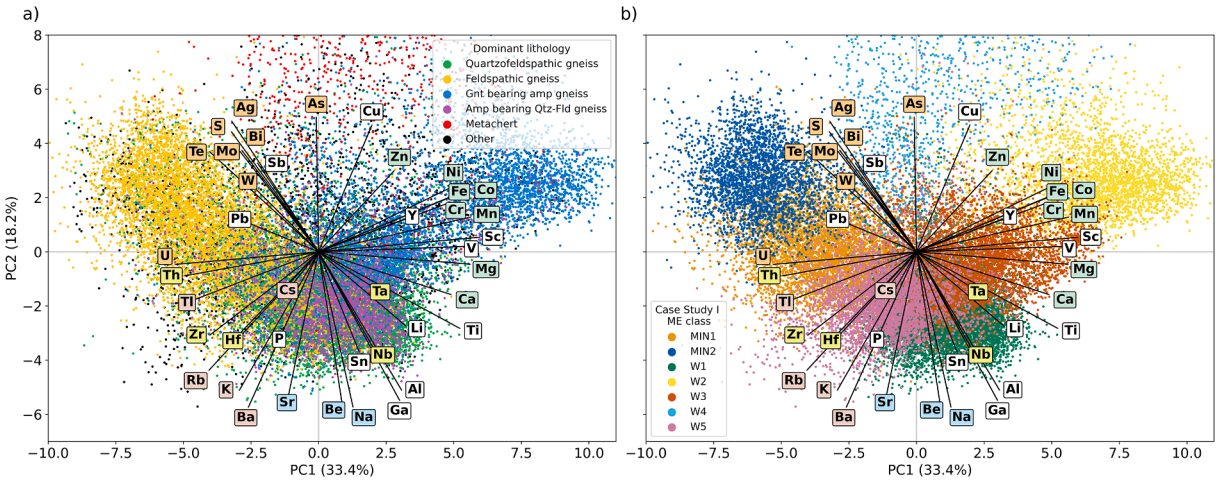

Fig. 7. Principal component biplot of clr-transformed geochemical data attributed by a) dominant lithology logged for each sample, and b) the clustering classes of Case Study I. Abbreviations: Gnt – garnet, Amp – amphibole, Qtz-Fld – quartzofeldspathic.

between the element groupings, geological features and the obtained classes. Fig. 7 shows a biplot of PC1-PC2 for the clr-transformed geochemical data coloured by the dominant lithology and the resulting clustering class. The element patterns of Fig. 6 match well with the logged lithology groups dominated by variably deformed gneissic rock types. The orientation of mafic rock indicating elements correspond well with garnet-bearing amphibolitic gneiss, and the mineralisation indicating elements match with the dominant feldspathic gneiss. Whereas a low PC2 indicate feldspar associations with more sodic or potassic alteration commonly seen in the quartzo-feldspathic gneiss units. Some clusters capture geochemical signatures related to lithological units quite well (Fig. 7b), however overlapping classes and lithological domains are also observed. The lithogeochemical identification resulting from the PCA and clustering is effective enough to separate commonly mineralised from unmineralised rock types. A further lithogeochemical separation of the dominant feldspathic gneiss clusters (MIN1 and MIN2) will be done in Case Study II (Section 5.2).

5.1.2. Geochemical discrimination

The easiest way to discriminate mineralised vs unmineralised classes (based on Au grade) is to look at the Au content of each sample within the classes. The Au data was attributed according to the clustering classes and viewed as statistical boxplots in Fig. 8. Three classes (W1, W2, W3) only contained samples with Au < 0.3 ppm and were denoted barren/unmineralised, and two classes (W4, W5) had >85% of the samples below 0.1 ppm Au (and only 2–5% was above the mine's cut-off grade of 0.3 ppm Au). The remaining two classes (MIN1, MIN2) relate more to the mineralisation signatures and will be clustered again in Section 5.2. The clustering itself did not consider the Au concentration as a variable, which means that the geochemical signatures of the resulting classes are distinct enough for mineralised and unmineralised signature separation, as will be discussed in Sections 5.1.3 and 5.1.4. Fig. 3 shows how the clustering classes spatially align with different geological units in a 100 m width Havana South cross-section. This demonstrates great spatial contiguity and validates that the obtained classes are also coherent with the geological interpretation.

To further assess the variability of the framework silicate mineralogy in the classes, the bulk rock ME data are plotted in an alkali-alumina molar ratio diagram (Fig. 9). This diagram shows the variations in bulk rock chemistry related to changes in mineral modal proportions per class (Davies and Whitehead, 2006). This diagram plots proportions of the mobile alkalies (Na and K) divided by the relatively immobile Al against each other. Various ideal mineralogical compositions of typical rock-forming minerals are also indicated, including the position of the least altered feldspathic gneiss and mafic garnet gneiss based upon logging. The position of samples plotting above the albite-K-feldspar tie

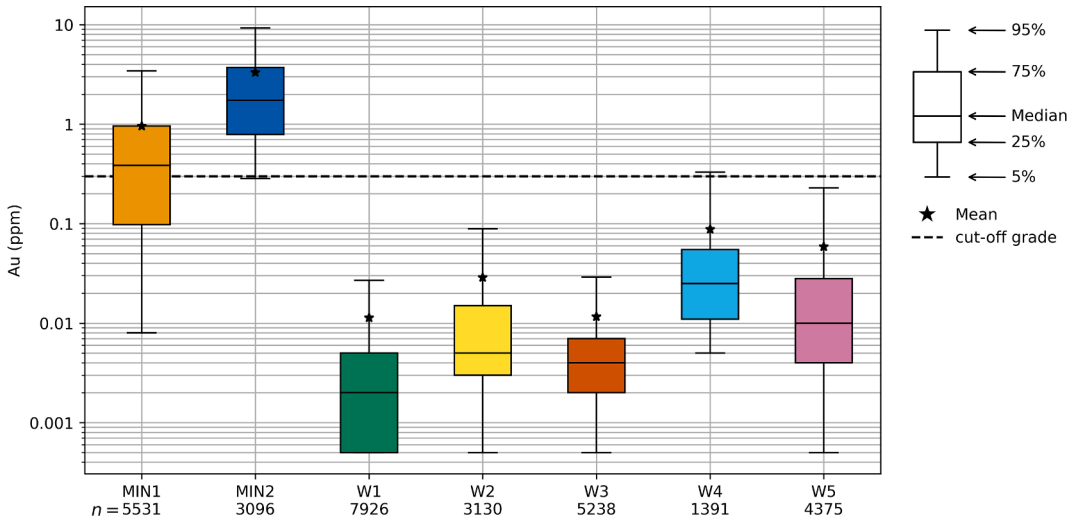

Fig. 8. Box and whisker plot of Au grade (ppm) for the clustering classes of Case Study I.

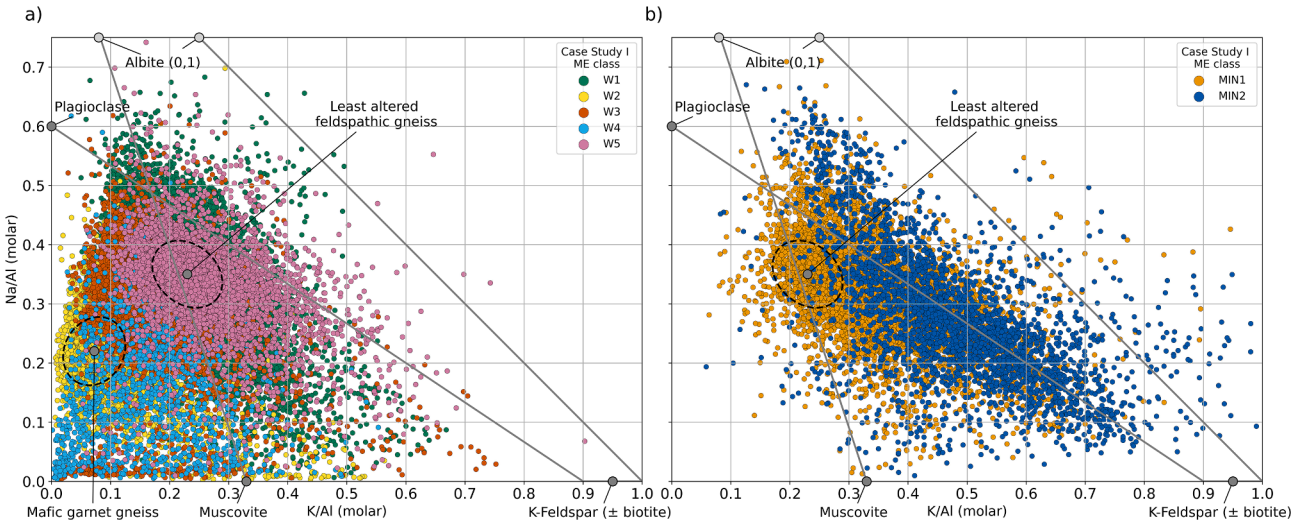

Fig. 9. Multi-element samples from Case Study I plotted to the alkali-alumina ratio plot to assess alteration phases, after Davies and Whitehead (2006), thematically attributed by clustering classes.

line likely reflects analytical measurement issues since one would not expect a natural sample to fall beyond this line.

The identified classes show a typical igneous and meta-igneous rock classification. The most felsic classes (MIN1/MIN2) are mineralised, showing a relative K enrichment and trend towards the K-feldspar ± biotite node in Fig. 9. The relatively unaltered feldspathic gneisses (class W5) are between $0.18 \leq K/Al \leq 0.3$ and $0.3 \leq Na/Al \leq 0.4$. Still felsic, but the more quartzofeldspathic gneisses (class W1), which are less sodic and a little more potassic, follow the albite-muscovite tie line indicating more sericite alteration. The more felsic/intermediate (class W3) and mafic (class W2) classes trend towards the origin. The highest point density of the garnet-bearing gneisses logged samples (mafic rocks) is between $0.02 \leq K/Al \leq 0.13$ and $0.15 \leq Na/Al \leq 0.27$. Finally, class W4 is closely related to a meta-ferruginous chert.

The following sections discuss the geochemical signature of each class and association with the alkali-alumina molar ratio diagram in more detail. The lithological descriptions of the classes are supported by the logged geology corresponding to the sample intervals (Fig. 7) and the observed plotting location in Fig. 9. Box and whisker plots of the elemental concentrations of samples found within each class for Case Study I can be found in Supplementary Material Fig. A.2.

5.1.3. Unmineralised material related classes (W1, W2, W3, W4 and W5)

Relative to the mineralised classes, the unmineralised classes show lower elemental concentrations of the mineralisation indicating elements, e.g., Au, S, Te, Tl, W, Mo, Bi, and Sb (Supplementary Material Fig. A.2). Therefore, the geochemical signature of W1, W2 and W3 represent non-gold bearing materials.

- Waste class 1 (W1, $n = 7{,}908$) is dominated by an unmineralised quartzofeldspathic gneiss signature (Fig. 7a) and relates to metamorphosed felsic volcaniclastics or intrusive units. The PC2 component is very low, indicating the feldspar association. Fig. 9 shows moderate Na/Al (molar) ratio values (0.2 to 0.5Na/Al) trending towards increasing modal proportions of plagioclase and albite, indicating a more sodic feldspar. Minor amounts of quartz-feldspar-bearing pegmatites also characterise this class. Geochemically, this class is characterised by a relative Na and K concentration almost equal to MIN1 and MIN2 but lacking the trace elements associated with mineralisation (Ag, As, Bi, Sb, Te).
- Waste class 2 (W2, $n = 3{,}123$) has a geochemical signature related to (mafic) garnet-bearing amphibolitic gneiss. It is the most mafic rock type demonstrated by a positive loading of PC1. This lithology is unmineralised (typically < 0.01 ppm Au) and does generally have chlorite +/- calcite alteration. This class also captured chlorite dominated schists and a few unsheared basalts and Proterozoic dolerites. The mafic rock signature is observed in the relatively higher concentrations of most major elements (Ca, Fe, Mn, Mg) and lower concentrations of K. This can also be seen in Fig. 9 since most W2 samples are trending towards the origin and are located near the mafic garnet gneiss node.
- Waste class 3 (W3, $n = 5{,}214$) has a geochemical signature that is a mixture of class W1 and W2. All samples fall between the mafic garnet gneiss and the least feldspathic gneiss node in Fig. 9. It mostly represents garnet-bearing amphibolitic and quartzofeldspathic gneiss rock types but also captures some biotite/chlorite dominated schists and saprolitic clays close to the surface (visibly distinct at Na/Al (molar) ≈ 0). Generally, these samples are less mafic, indicated by less chlorite alteration.

The geochemical signature of class W4 and W5 primarily represents unmineralised material with some trace Au mineralisation (2–5% of the class samples are above 0.3 ppm Au).

- Waste class 4 (W4, $n = 1{,}391$) samples all fall below the albite to muscovite tie line. This class has relatively higher Ag, As, Bi, Mo, Pb, Sb and Zn concentrations (high PC2) compared to the other unmineralised classes. Almost 54% of this material is logged as a *meta*-ferruginous chert (relatively high Fe and low Al), reflecting high modal proportions of pyrrhotite and (lesser) pyrite and magnetite (Hardwick, 2021).
- Waste class 5 (W5, $n = 4{,}375$) has a high point density directly at the least altered feldspathic gneiss node, similar to W1 (Fig. 9), representing samples with the least altered alkali signature. Compared to W1, this class has less quartz and is less sodic and more potassic, hence the trace mineralisation. Relative to MIN1/MIN2 and the mineralisation-related elements, this class lacks the higher Zr, Hf, Th, indicating a more distal spatial correlation with the gold system. Spatial contiguity indicates that these samples form part of the immediate hanging wall (Fig. 3).

5.1.4. Mineralisation associated classes (MIN1 and MIN2)

Mineralised class 1 (MIN1, $n = 5{,}531$) and class 2 (MIN2, $n = 3{,}096$) both have an Au-mineralised related geochemical signature, where MIN2 represents the high Au grade material (Fig. 8). The geochemical signature of both classes relates to a feldspathic gneiss, where MIN1 has

a more distinct quartz character (typically found in logging). These classes have similar Fe and K concentrations as the quartzofeldspathic gneiss classes (W1 and W5) but lower concentrations of Ca and Na. This higher relative proportion of Fe and K is accounted for by higher modal proportions of pyrite and K-feldspar (less biotite) and lower plagioclase proportions (Hardwick, 2021). Both classes are characterised by an enriched K/Al (molar) ratio, where MIN1 is generally a bit lower. Fig. 9 shows that the samples predominantly fall along the tie line between the ideal mineral composition of Ca-Na plagioclase and K-feldspar/biotite. This suggests that these classes reflect increasing potassic alteration from a relatively unaltered with primary Ca-Na feldspar to a highly altered and mineralised K-feldspar rich rock. The same is true for the increasing Au grade towards the K-feldspar node. The low-grade samples are more linked to lower K/Al (molar) ratios and are relatively plagioclase rich.

5.1.5. Summary of Case Study I

Geochemical data clustering from 30,687 samples revealed that two classes (n = 8,627) were predominantly related to the gold mineralisation signature found at TGM. The clustering did not take Au concentration into account as a variable, demonstrating that geochemical data is distinct enough for mineralised and unmineralised material to be discriminated. Furthermore, the approach is data-driven and automated hence repeatable classification can be done. Another approach to split mineralised and unmineralised material would be to use the logged lithology and Au grades. However, this may be complicated by the subjectivity of geological logging and the nuggety nature of Au assay data. Despite these limitations, the results showed that significant overlap was found between the defined classes and logged lithology, hence the classes can be used as a first pass lithogeochemical classification of mineralised and unmineralised material. In the next section, the two mineralised material classes are re-clustered to find geochemical signatures typically associated with comminution and recovery characteristics of mineralised material at TGM.

5.2. Case Study II: Interpretation of comminution and recovery parameters

The first case study showed the effectiveness of clustering geochemical data and how it could discriminate mineralised material from unmineralised material (waste). The second case study is a sequel to the previous case study and has the aim to find geochemical signatures typically associated with comminution and recovery characteristics of mineralised material at TGM. This part continues only with the indicated mineralised related material classes (MIN1 and MIN2) only since these are expected to dominate the processing stream. The samples (n=8,627) corresponding with these classes are selected and the original sample elemental concentrations are again clr-transformed and normalised.

5.2.1. Elemental patterns derived from PCA

PCA reduced the 41 element features to 26 PC features, and a new clustering was performed. Two more PCs are required to describe the 95% data variation compared to Case Study I. This is as expected because the samples are geochemically more similar and, therefore, more components are needed to explain the data variation. A visualisation of the scaled and ordered eigenvalues of PC1 and PC2 for all elements can be seen in Fig. 10. Note that a biplot similar to Fig. 7 would not have shown a separation based upon lithology since 82% of the samples were logged either as feldspathic gneiss (n = 5,726) or quartzofeldspathic gneiss (n = 1,344). See Supplementary Material Fig. A.3 for biplots of PC1-PC2 and PC1-PC3.

Fig. 10 shows that a positive PC1 is mostly related to elements that are indicative of mineralisation and dominated by positive loadings on U, Bi, Te, Sb, W, Mo, As, and S. The oxide bearing elements found (Ca, Ti, Mg, Al) are found at a lower PC1. A positive PC2 loading has a larger association with the mafic indicating elements (Ni, Cr, Co, Cu, Fe, Ag). However, this would in the felsic gneiss logged samples be more considered as metal associations. At a low PC2 are the relative immobile high field strength element (HFSE) pairs Hf and Zr, Nb and Ta, and low field strength elements Sr and Rb.

It is observed that this PC analysis is more focused on grouping samples with similar degrees of positive and negative relationships with given element eigenvectors together rather than separating major rock units from each other, as was found in Case Study I. This is the desired effect because most of the samples are mineralised and, therefore, clustering partitions will indicate geochemical differences due to the alteration and mineralisation. Ultimately resulting in different metallurgical responses. It is found that the mineralised material can best be partitioned in five clusters indicated by the peak and trough in the Silhouette score and Davies-Bouldin index score, respectively (Supplementary Material Figure A.1).

5.2.2. Geochemical signatures

To discuss the geochemical signatures of the classes, it is helpful to first look at the gold grade of the classes to find out which material classes have the highest chance of being processed. Analysing the classes for their gold content indicates that all classes have an average Au grade above the 0.3 ppm cut-off grade and have a high likelihood to be considered as run-of-mine material. Fig. 11 shows boxplots of the Au

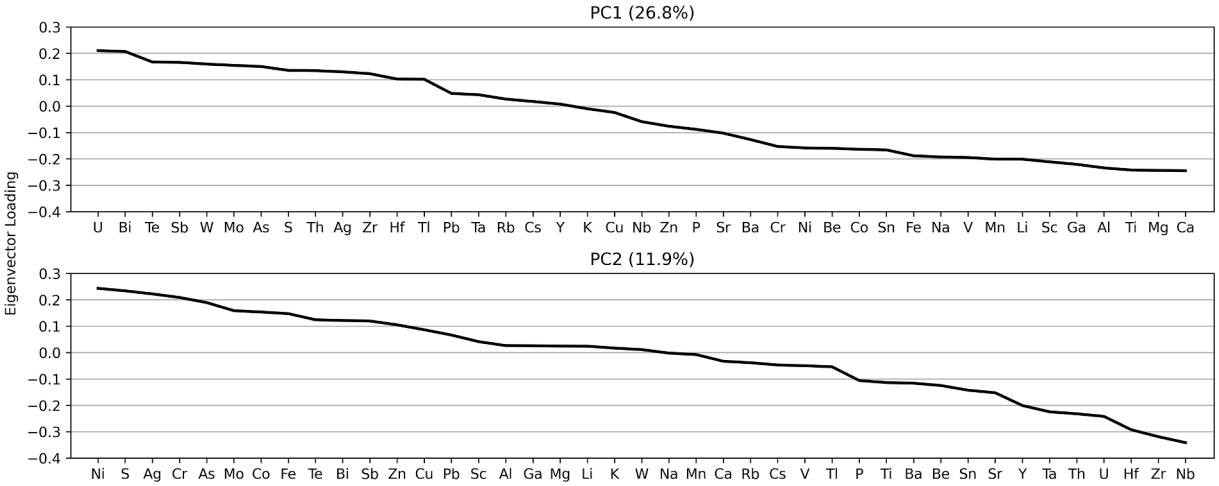

Fig. 10. Case Study II related scaled and ordered eigenvalues of PC1 and PC2 for all elements.

grade per class. The median Au grade of the mineralised waste or low grade (LG) class is 0.15 ppm; the marginal grade (MG) class is 0.54 ppm; high grade 1 (HG3) is 0.86 ppm; high grade 2 (HG2) is 1.33 ppm, and high grade 3 (HG1) is 2.63 ppm. Note that the average Au grade per class is higher than the median.

Medium and Lower-Grade mineralisation classes (MG, LG): Due to a large number of samples ($n = 30,687$) and the constraint of having only seven classes in Case Study I, there are still unmineralised samples not separated yet from the mineralised material since they have fairly similar geochemical characteristics as the mineralised feldspathic gneiss. These classes have notably minor or absent K-feldspar compared to the high-grade classes. Their composition is more plagioclase-bearing ± quartz with amphibole-biotite. These samples are commonly found in the immediate (un-mineralised) hanging wall and footwall lithologies.

Fig. 12a shows that the MG ($n = 1,882$) and LG ($n = 2,464$) samples plot the closest to the least altered feldspathic gneiss node, are mostly below the plagioclase-K-feldspar tie line, and slightly disperse towards the muscovite (LG) or K-feldspar (MG) node. These class signatures are more associated with increasing sericite-biotite-chlorite alteration. Fig. 13 shows that relative to the high-grade classes, MG and LG typically have lower concentrations in the ore elements associated with the sulphide and telluride minerals. Within the K-group elements (K, Ba, Rb, Cs, including Al) and oxide minerals (P, Th, U, Zr, Hf), it is evident that MG is more similar to HG2, whereas LG is similar to HG3.

High-grade classes (HG1, HG2, HG3): The three high-grade Au-mineralised classes all fall along the plagioclase – K-feldspar trend line (Fig. 12b), and these samples are predominantly logged as feldspathic gneiss or feldspathic pegmatites. HG3 ($n = 1,837$) has the lowest K/Al and highest Na/Al molar ratios and is partially still characterised by some sericite-chlorite alteration. HG2 ($n = 1,225$) and HG1 ($n = 1,219$) have increasing K/Al and decreasing Na/Al molar ratios and have a more abundant biotite-sericite or biotite-pyrite alteration. Hardwick (2021) discriminated that these higher K/Al molar ratios of the feldspathic gneiss units are more controlled by higher modal proportions of perthitic K-feldspar rather than by enrichment in biotite (since higher K/Al (molar) trends towards the K-feldspar node on an Al-K-Mg molar ternary plot). The mineral classification also ranges from phengite ± biotite with the highest gold grade (HG1) to increasingly chlorite-rich, muscovite-bearing domains associated with the lowest gold grade (HG3, but also still in MG and LG).

HG1 is the richest in K and S of the three classes. The main difference between these classes is their relative degree of enrichment in ore metals (Bi, Te, Tl, Ag, Sb, Mo, Th, U, W), where HG3 has the lowest relative proportions (Fig. 13). In terms of geochemistry, HG1 and HG3 are more alike. They both have higher concentrations in the transition metals (Co, Cr, Cu, Ni), whereas HG2 (and MG) has higher concentrations in the high field strength elements (Zr, Hf, Nb and Ta). Interestingly, 77% of HG1 samples are spatially located within the Boston Shaker domain.

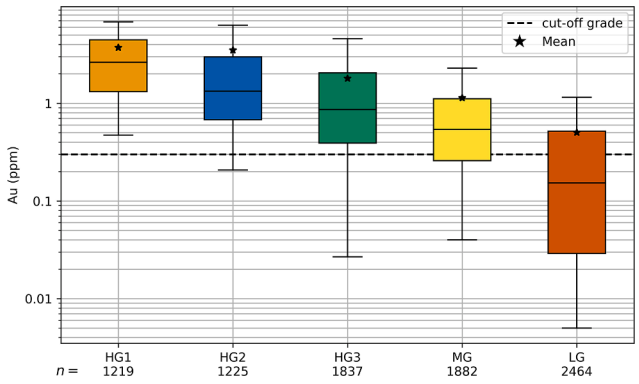

Fig. 11. Box and whisker plot of Au grade (ppm) for the clustering classes of Case Study II. HG: high grade, MG: marginal grade, LG: low grade.

This class demonstrates the known high-grade ore shoot characteristics (including biotite/pyrite alteration).

5.2.3. Spatial domains

The composites analysed for Equotip, BWi, Axb or recovery are typically gold grade and geologically-constrained metallurgical samples and thus incompletely reflect in-situ geochemical (and mineralogical) variability. In addition, not all available composites have complementary ME data. This makes it challenging to match the ME classes directly with the hardness proxies and explore their potential relationships. To increase collocated samples, all ME and hardness samples have been grouped according to their spatial location, i.e., per orebody and constructed domains. It is assumed that the geochemical class signatures would be fairly similar within such a domain, and there should be a relationship with the metallurgical test results. Traditionally, these domains came from Au grade resource modelling (≥0.3 ppm Au), but some have been split by the modelled faults to represent coherent geochemical domains better. Fig. 14 shows the spatially and geochemically constrained orebody estimation domains for the Tropicana Gold Mine. For example, between domain TP_3 and TP_4, there is a shear zone obliquely intersecting the line of mineralisation in E to SE direction (Blenkinsop and Doyle, 2014). This shear zone is associated with an alteration event and increased schistosity which affects the material hardness.

The proportion of each ME class within the domains is defined and shown in Fig. 15. This shows a spatial zonation of the ME class signatures, but also that the hanging wall and footwall of the different domains are geochemically distinct. In general, the clustering is effectively separating various geochemical and mineralogical associations from each other, characterising the different alteration and deformation events taking place with varying intensities, mineralogy and timings (Blenkinsop and Doyle, 2014). For example, at Boston Shaker, there is high Au grade material clustered in HG1, and then only lower grade samples in HG3 and relatively unmineralised material in LG. This indicates that the classes identify unique geochemical signatures associated with various mineralised fluid source compositions, alteration and resulting mineralogy.

Fig. 15 shows that the HG1 geochemical signature accounts for 36–58% of the Boston Shaker domains (green shaded), whereas HG1 is almost absent in the other domains. This characterises the biotite and pyrite dominated assemblages with an increased abundance of white mica in the K-feldspar (higher grade). Another large group of domains (HS_2, HS_3, HA_3, HA_4, TP_1-3, orange shaded) have on average 5% HG1, 22% HG2, 17% HG3, 31% MG and 25% LG. However, there is a switch in the proportion of MG and LG between the Havana and Havana South, and Tropicana domains. This fairly similar geochemical signature typically observed in the footwall lodes demonstrates the more plagioclase rich domains (typically lower grade and with chlorite being dominant over muscovite) with intermediate composition phengitic rock.

The hanging wall mineralisation lodes at Havana and Havana South (HS_1, HA_1 and HA_2, blue shaded) all have high HG3 (26–56%) with variable MG and LG, but absence of HG1 and HG2, indicating a high degree of geochemical similarities. These lodes are more phengite dominant with biotite ± quartz but also indicate more muscovite + chlorite in the alteration (larger proportion of MG and LG). These three domains are the shallowest mineralisation lenses (see Fig. 3, top feldspathic gneiss ore zone, Fig. 14b-c) found in the Havana and Havana South regions. Note that the number of samples ($n = 7,746$) in Fig. 15 is not equal to the Case Study II samples ($n = 8,627$) as the remaining samples were found outside the considered domains and ME samples or metallurgical test results were not sufficiently available for all domains.

5.2.4. Hardness and recovery attributes

During (pre-)feasibility studies, these domains have been adequately sampled to determine the hardness and recovery parameters. Fig. 16

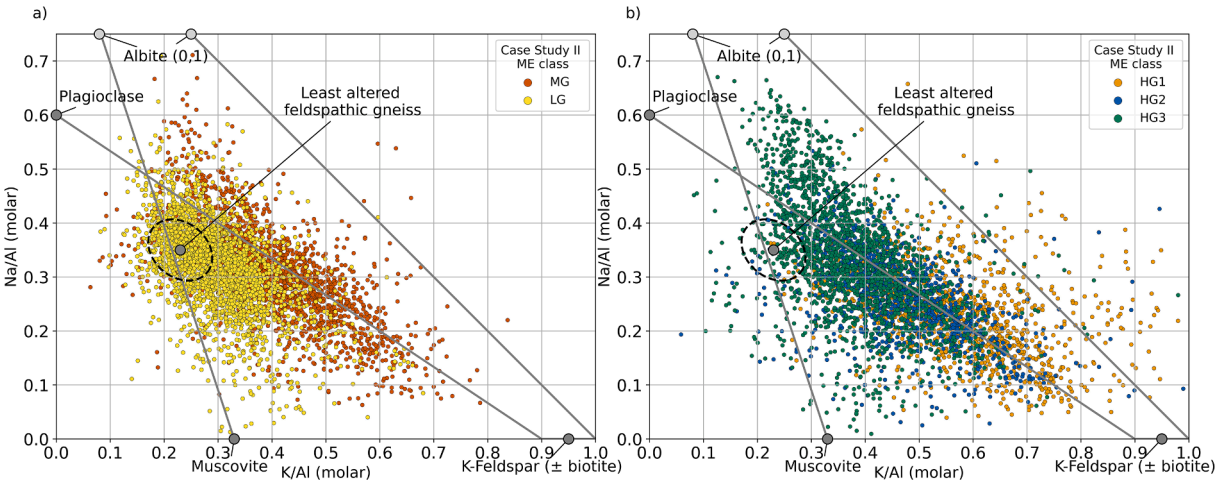

Fig. 12. Multi-element samples from Case Study II plotted to the alkali-alumina ratio plot, after Davies and Whitehead (2006), thematically attributed by clustering classes.

shows the average ± 1 SD BWi (kWh/t), Axb, Equotip hardness (Leeb), and 48-hour leach recovery composite data for the considered domains. This analysis indicates that domains with similar geochemical signatures also frequently have similar material hardness and 48-hour leach recovery behaviour. In addition, it is now possible to propose an explanation for the variations (if any) in the metallurgical proxies.

The following results are derived from the combined domain-based ME class proportion and Equotip hardness, BWi and Axb metallurgical test results split per domain (Fig. 16):

- HS_1, HA_1 and HA_2 (blue shaded) have similar geochemical signatures (high HG3 + variable MG/LG). The BWi (18.4 kWh/t) and Axb (41.7) of HS_1 is lower and higher, respectively, compared to HA_1 (BWi: 20.1 kWh/t, Axb: 30.5) and HA_2 (BWi: 20.3 kWh/t, Axb: 33.1). These domains are rich in the transition metals (Cr, Ni) and poor in Hf, Zr, Nb and Ta, concentrations demonstrating the expected geochemical signature of HG2 (and LG). These domain samples have a low K/Al and a high Na/Al ratio, indicating less clay and thus harder characteristics (trending more towards the albite node instead of K-feldspar). HS_1 may have a lower hardness due to the shear zone separating Havana South and Havana having changed the feldspathic gneiss textures. This domain also has an increasing proportion of white mica with chlorite alteration.
- Domain HS_2, HS_3, HA_3, HA_4 and TP_1-3 (orange shaded) are generally quite hard due to larger proportions of plagioclase rather than K-feldspars. This, in conjunction with the presence of quartz (and minor garnets), make these relatively hard domains. The HS_2 and HS_3 composite samples are closer to the surface and affected by weathering resulting in softer material (<18 kWh/t). The other domain composites have a fairly consistent BWi of 19.8 ± 1.2 kWh/t. A gradational trend of slightly increasing (reduced hardness) Axb from 34 to 39 and decreasing (reduced hardness) Leeb from 800 to 760 is observed as one transition towards domain TP_3, where it abruptly changes due large "Jigger" shear zone (right-hand side of Fig. 14a) separating zone TP_3 and TP_4. TP_4 returns a much lower BWi (16.6 kWh/t), higher Axb (45.5) and lower Leeb values (742), indicating much softer rock. This domain (TP_4) is associated with a strongly (sheared) phengitic white mica-affiliated rock type, exhibiting significantly softer hardness and elevated recovery. There is also a change of class proportion for this domain, where an increased HG1 (20%, high molar K/Al) and slightly higher HG2 (34.1%) proportion present relative to its neighbouring domain TP_3.
- The Boston Shaker domains (green shaded) have an elevated (HG1) proportion related to a more perthitic K-feldspar rich (increased K/Al) rock. The increased proportion of white mica and biotite tend to soften (BWi: 18.5 ± 1.0 kWh/t) these domains compared to plagioclase feldspar dominated domains (more HG3). Within Boston Shaker, the most notable difference is in the hanging wall domain BS_1, which has increased HG2 (16%) and decreased LG (18.5%) class proportions. This is a more sheared and phengitic white mica-affiliated domain exhibiting similar characteristics as TP_4 (high Axb).

The following results are derived from the combined domain-based ME class proportion and 48-hour leach recovery metallurgical test results split per domain (Fig. 14):

- The 48-hour leach recovery results from domains HA_3, HA_4 and TP_1-4 (orange shaded) are quite variable. TP_2 and TP_4 have a relatively high recovery, around 93%, whereas the recovery of the others is between 88.2 and 89.9%. A possible explanation for the lower recovery in these domains is the evidence of preg-robbing eluded to by Baker (2020). The cause is unknown as there is usually very little organic carbon in the ore to explain the effects by adsorption into carbonaceous material. The effects may be caused by the reduction of gold onto arsenopyrite or possible chalcopyrite surfaces, but this is unlikely due to the low As concentration (~3.5 ppm) (Baker, 2020).
- Unfortunately, the increased 48-hour leach recovery for HS_1 (93%), HA_5 (94%), TP_2 (93.4%) and TP_4 (93.1%) cannot be explained by similarity of the geochemical class proportions (Fig. 15). HS_1 has a larger HG3 proportion, and these samples are trending towards the albite node on the alkali-alumina plot and have lower S and Fe. Whereas TP_4 has significantly higher K/Al (molar) ratios (and HG1), higher S and Fe, and these samples are more trending towards the perthite K-feldspar node. Especially HS_1, HA_5 and TP_2 have in common that they are quite shallow and that the tested material types are predominantly lower saprolite and transitional saprolite rock compared to the fresh rock parts of, for example, the Boston Shaker domains (green shaded).
- The recovery data associated with higher proportions of HG1 domains (Boston Shaker) reflect observations seen at the mine site; elevated As, Te and S material (HG1, Fig. 13) leaches poorly (89.3 – 92.5%) under standard conditions and will most likely increase the cyanide consumption. These elevated elemental concentrations would suggest increasing amounts of gold associated with tellurides and arsenopyrite, affecting the recovery. The increased sulphur (a known cyanocide) may cause higher cyanide demand. This is typically combated by increased oxygen and lead nitrate demand. The NaCN consumption for the Boston Shaker domains (high HG1 and

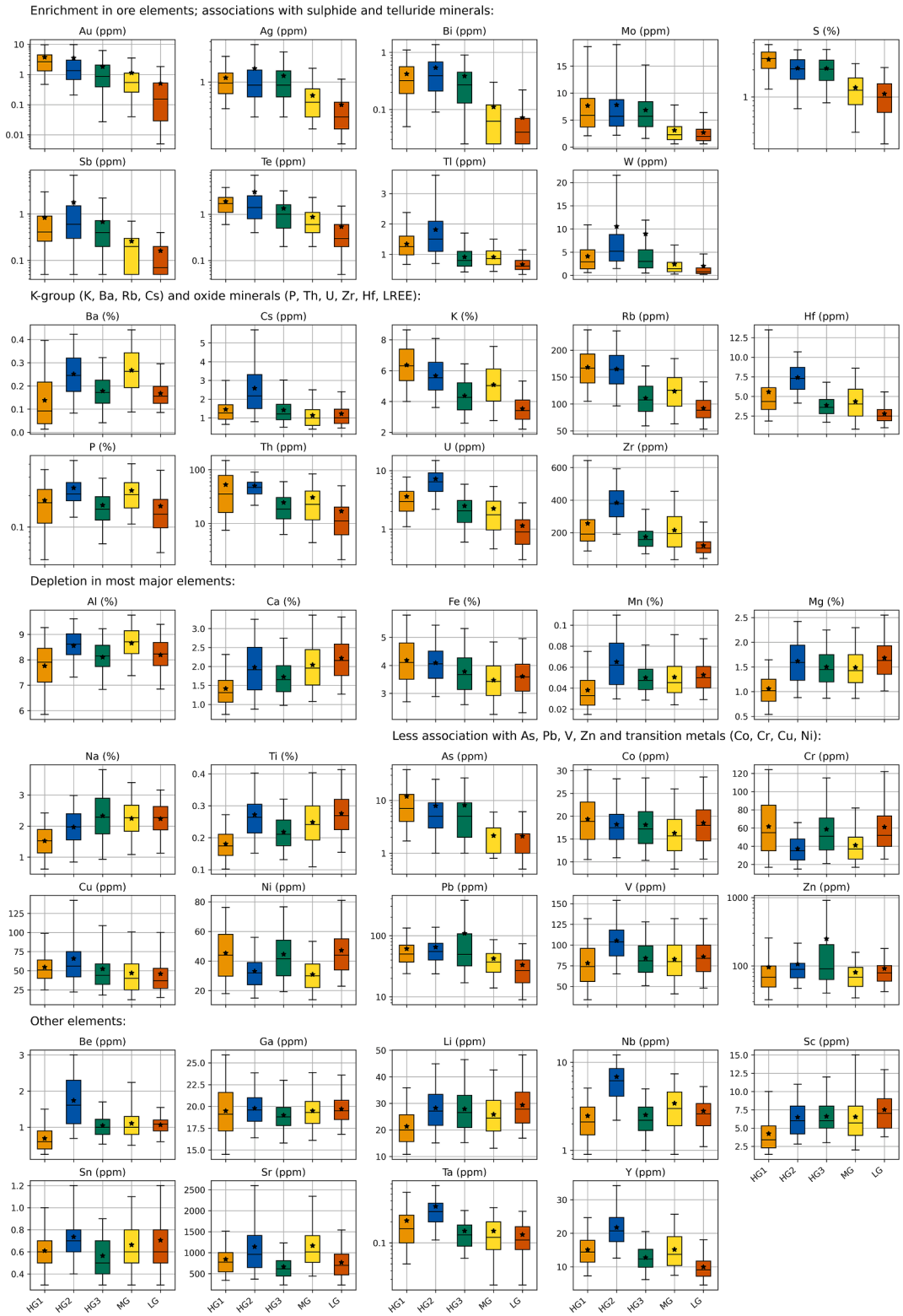

Fig. 13. Box and whisker plots of elemental concentrations of Case Study II samples. See Fig. 8 for an explanation of the box and whisker parameters and Fig. 11 for the number of samples per class.

sulphur) is almost double (0.48 ± 0.15 kg/t) compared to the other domains (0.25 ± 0.23 kg/t). The lime consumption is much lower (0.67 ± 0.19 kg/t) than the other domains (2.53 ± 1.10 kg/t).

5.2.5. *Summary of Case Study II*

This case study showed that clustering of mineralised material is possible and generated classes with distinct geochemical, mineralogical and physical attributes. Including the spatial context of the ME data proved to give valuable insight into the coexistence of various classes and resulting metallurgical properties. For instance, similar geochemical class signatures were found across multiple orebodies. Additionally, there are various effects of known structural control events (with

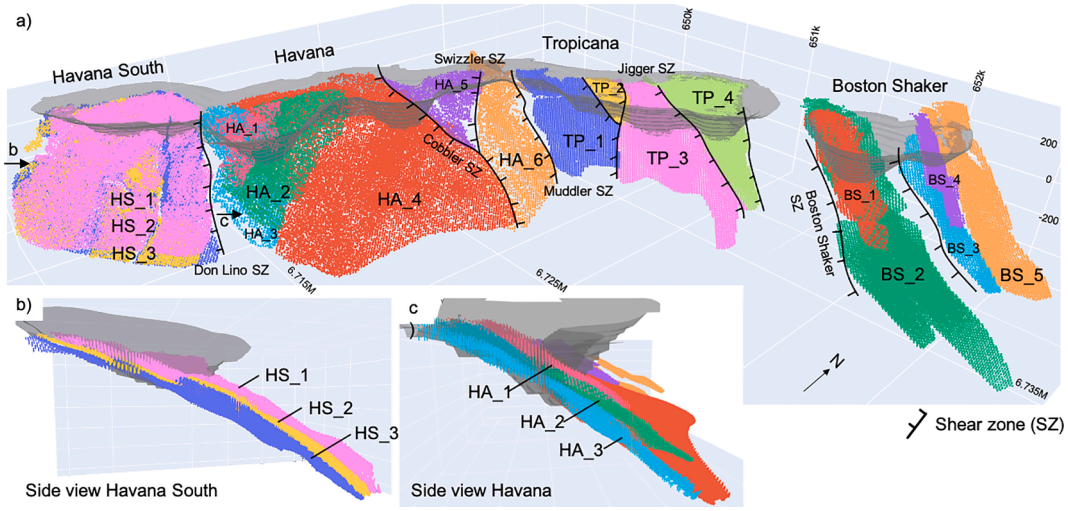

Fig. 14. a) Overview of the selected orebody domains (≥0.3 ppm Au) for the Tropicana Gold Mine (mineralisation over 5 km strike length), b) side view of Havana South, and c) side view of Havana domains. GDA/UTM grid.

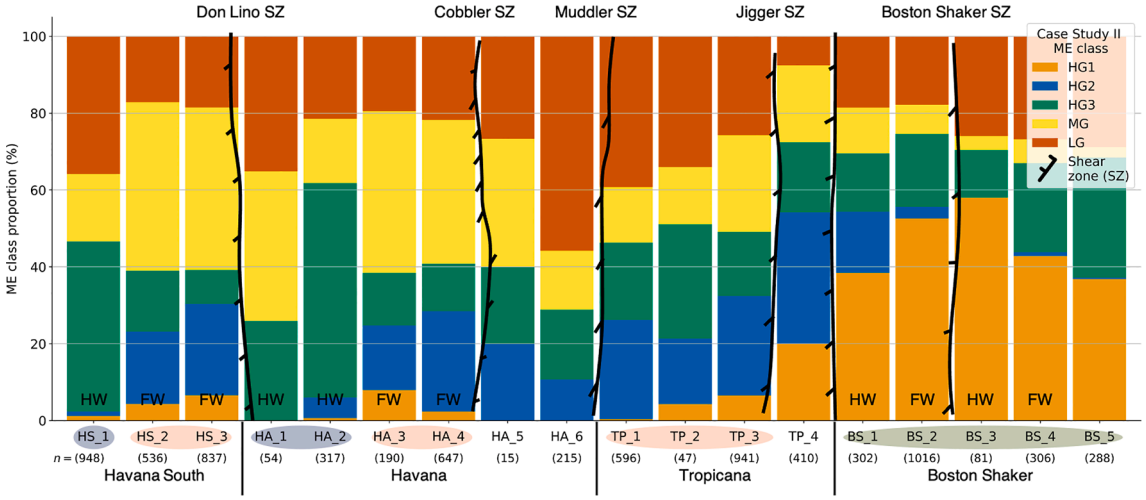

Fig. 15. ME class proportions (Case Study II) typically found in selected Tropicana Gold Mine orebody domains (x-axis). The shaded domains have roughly similar geochemical signatures. Also, see Fig. 14 for the spatial configuration, SZ = shear zone, HW = hanging wall, FW = footwall.

alteration stages) observed within the domain signature, such as changes in the geology, alteration assemblage and mineralisation. The resulting material hardness can typically be explained by the class compositions found within domains, whereas the recovery tends to be explanatory with elevated or depleted elemental concentrations.

6. Discussion

The shear zone-controlled alteration of the protolith towards the mineralised assemblages was previously described by Crawford and Doyle (2016). Geochemically, these processes relate quite well with the observed HG1/HG3 and HG2/MG class properties. Crawford and Doyle (2016) described a decrease in SiO2, major elements (Fe, Mg, Ca, and Ti) and transition metals (V, Ni, Cr, Co, and Zn) accompanied by a strong increase in K-group elements in the shear zone assemblages. This character is more prevalent in HG2/MG than in HG1/HG3 (Fig. 13). Mineralogically, this increase in K-group elements is reflected by the stabilisation of abundant K-feldspar, biotite and white mica. Then, the decrease in abundance of the major elements and transition metals is reflected by the destruction of hornblende, augite, and Fe-Ti oxides in the protolith gneisses as the new alteration assemblage quartz-K-feldspar-biotite-pyrite stabilised in the shear zones (Crawford and Doyle, 2016). The formation of the alteration assemblage was also accompanied by the breakdown of mafic minerals in the protolith gneisses. Some of the Fe, Mg, and Ti released were trapped in the pyrite and lower-Ti biotite, however, the mass balance of Ti is not fully resolved and not completely reported by Crawford and Doyle (2016).

The shear zone assemblage of the TGM deposit also has implications for the physical properties of the rocks. For example, there is an abrupt change in hardness of TP_4 (BWi: 16.6 ± 1.2 kWh/t, Axb: 45.4 ± 7.5) compared to TP_3 (BWi: 20.1 ± 1.5 kWh/t, Axb: 37.7 ± 5.1) caused by the "Jigger" shear zone crosscutting the deposit (as shown in Fig. 16). At TP_4, the decrease in hardness is accompanied by an increase in HG1 and HG2, reflected mineralogically by a strongly (sheared, schist-like) phengitic white mica-affiliated rock type. This suggests that the proximal distance from a shear zone has additional influence on the material hardness and probably the particle size and recovery. This hypothesis is tested by analysing the dilatancy around the shear zones, which commonly reflect the degree to which fluid-dominated or rock-buffered processes acted (Hodkiewicz et al., 2008). The dilatancy implies that during the feldspar-to-mica reactions occurring in these fault zones, the released silica may have precipitated in these dilatant sites. This

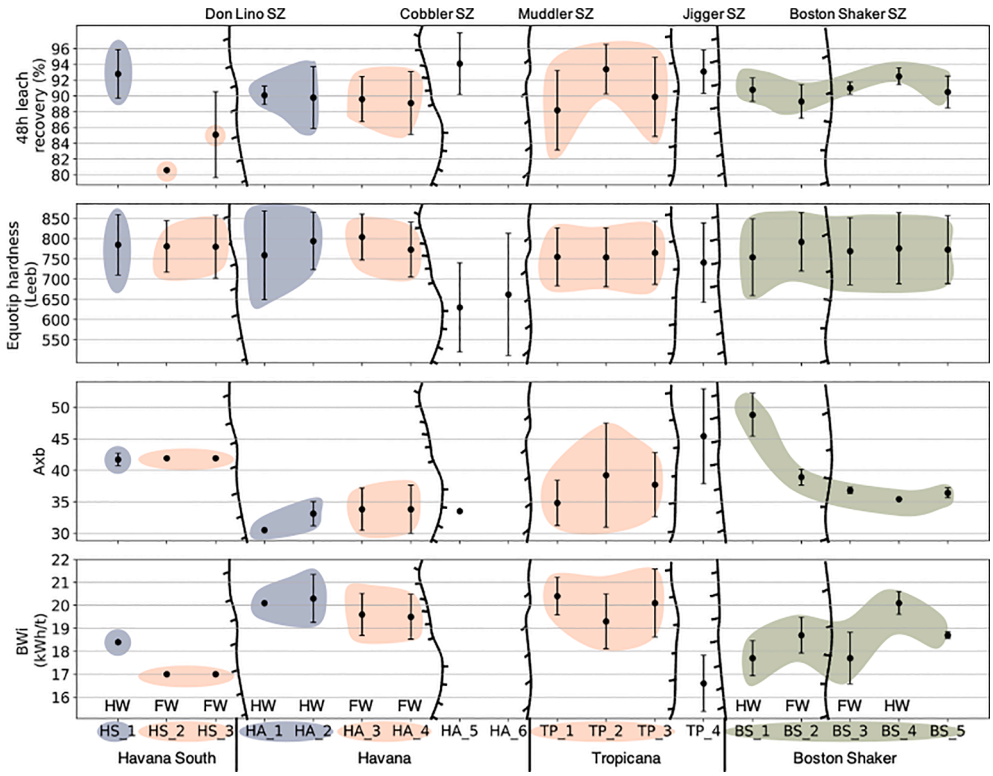

Fig. 16. Average BWi, Axb, Equotip and 48-hour leach recovery composite data for the considered spatial domains. The shaded regions indicate domains with shared geochemical signatures (Fig. 15). Vertical lines indicate displacements of the orebodies by minor or major faults (also see Fig. 14). SZ = shear zone, HW = hanging wall, FW = footwall.

increased the fault rock strength by cement hardening and reduced its permeability (Wibberley, 1999).

This process has a significant impact on the material hardness and is observed across various domains. For example, a related and noticeable geochemical difference can be found within Tropicana. TP_4 has a higher average molar K/Al (0.47 ± 0.14) ratio and thus implies a more perthitic K-feldspar feldspathic gneiss than the more plagioclase rich feldspathic gneiss at TP_3 (K/Al ratio: 0.37 ± 0.12). Another shear zone that can be considered to test this hypothesis is the Boston Shaker shear zone. BS_1 has a similar high molar K/Al ratio and equally soft rock characteristics (BWi: 17.7 ± 0.8 kWh/t, Axb: 48.8 ± 3.4) as TP_4. In this domain, the perthite-rich feldspathic gneiss progressed from a clast supported breccia to matrix-supported breccia (Hardwick, 2021). It is evident that similar strength-controlling mechanisms occurred at other high-intensity strain domains and that each had specific implications on the resulting geochemistry and mineralogy, hence variations in the class proportions of the domains.

Given the geochemical differences between the classes, it is expected that the resulting rock hardness is a combination of various rock properties. It must be mentioned that the authors are aware of the non-additive properties of material hardness. The individual or cumulative effect of the following three proposed hardness relationships is unknown.

- The HG2 and MG classes are characterised by elevated HFSE concentrations (Zr, Hf, Nb, Ta). These elements are usually found in accessory minerals of high density (apatite, zircon) and can indicate fractional crystallisation of felsic alkaline magmas (Motoki et al., 2015). Therefore, these elevated proportions are expected to contribute to the hardness observed in, for example, HS_2, HA_3, HA_4 and TP_1-3.
- There is a large difference between the BWi and Axb of the blue shaded domains (HA_1, HA_2 and HS_1) and green shaded domains (Boston Shaker). This transition from dominance in HG3 (blue domains) to HG1 (green domains) is related to an increase in the modal proportion of perthitic K-feldspar (higher K/Al molar ratio). As a result, there is less energy required to grind the rocks at Boston Shaker. However, the Leeb hardness indicates almost similar rock characteristics. The contradiction of soft/hard indications of the BWi, Axb and Equotip rebound hardness (Leeb) tests may represent the nature of the tests and their relation to hard or brittle material. For example, BWi and Axb are destructive tests, whereas Equotip is a non-destructive test. Equotip hardness generally reflects the mineralogical rebound hardness based on the observed matrix crystal structure, whereas the BWi reflects the combined resistance to abrasion and impact, and Axb the compression resistance. Typically, the Leeb value becomes lower as the rocks are more sheared (such as in TP_4 or HA_5) because of the development of a more dominant fabric and the conversion of feldspar to sericite (mica). Hence, the chances of hitting a hard mineral grain (feldspar, quartz, garnet) diminishes and hitting a fine, softer matrix material increases. Thus, the class composition of Boston Shaker results in an easier to grind rock type, however, within the crystal matrix, there are equally hard grains observed with Equotip hardness testing as in the blue shaded domains.
- At Tropicana, coarse-grained feldspathic pegmatite is similar to the feldspathic gneiss in terms of major element concentration and is therefore not discriminated in this study. However, the main differences between the two lithologies are in the grain size (>4 mm) of framework silicates rather than changes in modal mineralogy (Hardwick, 2021). Pegmatites tend to be composed of relatively hard minerals, so contributing to the observed and measured hardness of the composites. Pegmatites are more frequently logged in MG (n = 249) and LG (n = 125) samples compared to HG1 (n = 107), HG2 (n = 37), and HG3 (n = 56) and therefore expected to contribute more to the hardness observed in the high MG and LG domains.

Understanding the deleterious characteristics of the ore, such as oxygen or cyanide consumers, preg-robbers/borrowers, or passivation due to tellurides is a complex undertaking and requires extensive testing (Coetzee et al., 2011). The following examples are observed at the mine and could be linked with the ME class or domain characteristics. For instance, there is an inverse relationship between cyanide and lime especially observed in the blue and green shaded domains. The blue shaded domains (HA_1, HA_2 and HS_1) have a high HG3 with variable MG and LG, but absence of HG1 and HG2, characterising a high lime consumption (>2.2 kg/t) and low cyanide need (<0.31 kg/t). The following two observations may explain this high lime need. Firstly, these classes have proportionally more Mg and clays in the representing material, which tend to decrease the pH resulting in an increased lime consumption (du Plessis et al., 2021). Secondly, HG3 typically has higher concentrations in metal grades (Ni, Zn, Pb, Cu) and lower or equal concentrations of ore elements (Ag, Bi, Mo, Sb) than HG1. These metal-bearing minerals tend to reduce leach kinetics and lower the pH and must be combated by adding lime but less NaCN.

7. Conclusions

This paper presented an agglomerative hierarchical clustering approach with multi-element (ME) geochemical data from the Tropicana Gold Mine, Australia. This approach was very effective in classifying the logged lithology, alteration or mineralisation and could, for example, discriminate unmineralised, marginal-grade and high-grade gold classes. The work involved exploring classes for their unique geochemical signature, relating classes with their typical comminution and recovery parameters, and explaining the observed processing attributes and their cause.

The paper started with an extensive data quality assurance and successfully demonstrated how an industry scale four-acid digestion dataset could be cleaned to ensure no significant bias between inter-laboratory and intralaboratory measurements. Case Study I presented the separation of 30,687 ME samples in seven classes through clustering. The clustering was primarily driven by the dominant mafic, felsic, garnet-bearing, garnet-absent, chert or quartz containing geochemical signatures of the gneissic rock found in each class. This demonstrated that the classes picked up different original host rocks and alteration assemblages seen across domains. The two gold-bearing classes were easily separated from the others (not based upon Au). Case Study II (n = 8,627 samples) continued with the two mineralised classes and demonstrated further partitioning in five classes: three high-grade classes, one marginal-grade class and one low-grade class. This clustering placed a greater emphasis on grouping assemblages with relative increased or decreased elemental concentrations rather than separating major rock units.

The geochemical data were spatially combined with metallurgical test results by considering all results within a constrained $\geq$ 0.3 ppm Au grade resource domain. This bridged the gap between these two different datasets. The geochemical signatures of the classes and domains were then used to explain the differences in observed breakage properties (Leeb, BWi, Axb) and recoveries. This new approach of interpreting comminution and recovery related parameters demonstrated the benefits of material fingerprinting and suggests including mineralogical data in future to enhance results. Additionally, it would be beneficial if an adequate metallurgical test for each combination of geochemical composition and spatial (sub)domain was undertaken to improve understanding of the hardness and recovery characteristics. Future research will focus on increasing the sample representativity and include additional spatial context.

Funding

This research did not receive any specific grant from funding agencies in the public, commercial, or not-for-profit sectors. AngloGold Ashanti Ltd. provided access to data.

CRediT authorship contribution statement

Jeroen R. van Duijvenbode: Conceptualization, Methodology, Software, Investigation, Writing – original draft, Visualization. **Louis M. Cloete:** Conceptualization, Methodology, Validation, Resources, Writing – review & editing. **Masoud S. Shishvan:** Conceptualization, Methodology, Validation, Supervision, Writing – review & editing. **Mike W.N. Buxton:** Conceptualization, Methodology, Validation, Supervision, Writing – review & editing.

Declaration of Competing Interest

The authors declare that they have no known competing financial interests or personal relationships that could have appeared to influence the work reported in this paper.

Acknowledgement

The authors are thankful to AngloGold Ashanti Ltd. for permission to publish the outputs of the research. Stephen Brown, Tony Roach and Rodney Berrell are thanked for helpful reviews, which improved the paper. Tom Wambeke is acknowledged for assistance in conceptualising the topic and providing the datasets. The anonymous reviewers and Michael Gazley are thanked for their constructive reviews, which improved the paper.

Appendix A. Supplementary data

Supplementary data to this article can be found online at https://doi.org/10.1016/j.mineng.2022.107612.

References

Aggarwal, C.C., Reddy, C.K., *Data Clustering. Algorithms and Applications*. 2014, Taylor & Francis Group, London.

Aitchison, J., 1986. The statistical analysis of compositional data. In Monographs on Statistics and Applied Probability. Chapman & Hall, London.

Aitchison, J., 1999. Logratios and Natural Laws in Compositional Data Analysis. Math. Geol. 31 (5), 563–580. https://doi.org/10.1023/a:1007568008032.

Baker, S., 2020. Tropicana Gold Mine Havana. AngloGold Ashanti Ltd.

Bhuiyan, M., Esmaieli, K., Ordóñez-Calderón, J.C., 2019. Application of Data Analytics Techniques to Establish Geometallurgical Relationships to Bond Work Index at the Paracutu Mine Minas Gerais, Brazil. Miner. 9 (5) https://doi.org/10.3390/min9050302.

Blenkinsop, T.G., Doyle, M.G., 2014. Structural controls on gold mineralization on the margin of the Yilgarn craton, Albany-Fraser orogen: The Tropicana deposit, Western Australia. J. Struct. Geol. 67, 189–204. https://doi.org/10.1016/j.jsg.2014.01.013.

Brauhart, C.W., 2019. The role of geochemistry in understanding mineral systems. ASEG Extended Abstracts 2019 (1), 1–5. https://doi.org/10.1080/22020586.2019.12072914.

Caciagli, N., 2016. Multielement Geochemical Modelling for Mine Planning: Case Study from an Epithermal Gold Deposit. In: Martín-Fernández, J.A., Thió-Henestrosa, S. (Eds.), Compositional Data Analysis. Springer International Publishing, Cham, pp. 45–61.

Carranza, E.J.M., 2011. Analysis and mapping of geochemical anomalies using logratio-transformed stream sediment data with censored values. J. Geochem. Explor. 110 (2), 167–185. https://doi.org/10.1016/j.gexplo.2011.05.007.

Coetzee, L.L., Theron, S.J., Martin, G.J., van der Merwe, J., Stanek, T.A., 2011. Modern gold deportment and its application to industry. SGS Minerals Services Miner. Eng.. https://doi.org/10.1016/j.mineng.2010.09.001.

Crawford, A.J., Doyle, M.G., 2016. Granulite-Hosted Gold: Tectonic Setting and Lithogeochemistry of the Tropicana Deposit, Western Australia. Econ. Geol. 111 (2), 395–420. https://doi.org/10.2113/econgeo.111.2.395.

CSA Global Canada Geoscience Ltd, 2018. Integrated Assessment of Regional Stream-Sediment Geochemistry for Metallic Deposits in Northwestern British Columbia (Parts of NTS 093, 094, 103, 104). Canada, CSA Global Canada Geoscience Ltd, Vancouver, Canada.

Davies, J.F., Whitehead, R.E., 2006. Alkali-Alumina and MgO-Alumina Molar Ratios of Altered and Unaltered Rhyolites. Explor. Min. Geol. 15 (1–2), 75–88. https://doi.org/10.2113/gsemg.15.1-2.75.

Dominy, S., O'Connor, L., Parbhakar-Fox, A., Glass, H., Purevgerel, S., 2018. Geometallurgy—A Route to More Resilient Mine Operations. Minerals 8 (12). https://doi.org/10.3390/min8120560.

du Plessis, C.A., Lambert, H., Gärtner, R.S., Ingram, K., Slabbert, W., Eksteen, J.J., 2021. Lime use in gold processing – A review. Miner. Eng. 174. https://doi.org/10.1016/j.mineng.2021.107231.

Escolme, A., Berry, R.F., Hunt, J., Halley, S., Potma, W., 2019. Predictive Models of Mineralogy from Whole-Rock Assay Data: Case Study from the Productora Cu-Au-Mo Deposit, Chile. Econ. Geol. 114 (8), 1513–1542. https://doi.org/10.5382/econgeo.2019.4650.

Gaillard, N., Williams-Jones, A.E., Clark, J.R., Lypaczewski, P., Salvi, S., Perrouty, S., Piette-Lauzière, N., Guilmette, C., Linnen, R.L., 2018. Mica composition as a vector to gold mineralization: Deciphering hydrothermal and metamorphic effects in the Malartic district, Quebec. Ore Geol. Rev. 95, 789–820. https://doi.org/10.1016/j.oregeorev.2018.02.009.

Gazley, M., Collins, K., Roberston, J., Hines, B., Fisher, L., McFarlane, A., 2015. Application of principal component analysis and cluster analysis to mineral exploration and mine geology, In *AusIMM New Zealand branch annual conference*. Dunedin New Zealand 131–139. http://hdl.handle.net/102.100.100/92108?index=1.

Grunsky, E.C., Caritat, P.d., 2020. State-of-the-art analysis of geochemical data for mineral exploration. Geochem. Explor. Environ. Anal. 20 (2), 217–232. https://doi.org/10.1144/geochem2019-031.

Grunsky, E.C., Smee, B.W., 1999. The differentiation of soil types and mineralization from multi-element geochemistry using multivariate methods and digital topography. J. Geochem. Explor. 67 (1–3), 287–299. https://doi.org/10.1016/s0375-6742(99)00054-0.

Halley, S., 2020. Mapping Magmatic and Hydrothermal Processes from Routine Exploration Geochemical Analyses. Econ. Geol. 115 (3), 489–503. https://doi.org/10.5382/econgeo.4722.

Hardwick, B., 2021. Mineralised textures at the Tropicana gold mine: Implications for the genetic model and deportment of gold. University of Tasmania.

Hill, E.J., Pearce, M.A., Stromberg, J.M., 2020. Improving Automated Geological Logging of Drill Holes by Incorporating Multiscale Spatial Methods. Math. Geosci. 53 (1), 21–53. https://doi.org/10.1007/s11004-020-09859-0.

Hodkiewicz, P.F., Groves, D.I., Davidson, G.J., Weinberg, R.F., Hagemann, S.G., 2008. Influence of structural setting on sulphur isotopes in Archean orogenic gold deposits, Eastern Goldfields Province, Yilgarn, Western Australia. Mineralium Deposita 44 (2), 129–150. https://doi.org/10.1007/s00126-008-0211-5.

Hood, S.B., Cracknell, M.J., Gazley, M.F., Reading, A.M., 2019. Element mobility and spatial zonation associated with the Archean Hamlet orogenic Au deposit, Western Australia: Implications for fluid pathways in shear zones. Chem. Geol. 514, 10–26. https://doi.org/10.1016/j.chemgeo.2019.03.022.

Horwitz, W., Albert, R., 2006. The Horwitz ratio (HorRat): A useful index of method performance with respect to precision. J AOAC Int 89 (4), 1095–1109.

Hunt, J.A., Berry, R.F., 2017. Geological Contributions to Geometallurgy: A Review. Geosci. Can. 44 (3), 103–118. https://doi.org/10.12789/geocanj.2017.44.121.

Keeney, L., 2010. The Development of a Novel Method for Integrating Geometallurgical Mapping and Orebody Mapping. University of Queensland, Brisbane, Australia, p. 324.

Lamberg, P., 2011. Particles - the bridge between geology and metallurgy.

Lynch, A., *Comminution Handbook*. 2015, The Australian Institute of Mining and Metallurgy.

Madenova, Y., Madani, N., 2021. Application of Gaussian Mixture Model and Geostatistical Co-simulation for Resource Modeling of Geometallurgical Variables. Nat. Resour. Res. 30 (2), 1199–1228. https://doi.org/10.1007/s11053-020-09802-4.

Martín-Fernández, J.A., Hron, K., Templ, M., Filzmoser, P., Palarea-Albaladejo, J., 2012. Model-based replacement of rounded zeros in compositional data: Classical and robust approaches. Comput. Stat. Data Anal. 56 (9), 2688–2704. https://doi.org/10.1016/j.csda.2012.02.012.

Motoki, A., Sichel, S.E., Vargas, T., Melo, D.P., Motoki, K.F., 2015. Geochemical behaviour of trace elements during fractional crystallization and crustal assimilation of the felsic alkaline magmas of the state of Rio de Janeiro, Brazil. An Acad Bras Cienc 87 (4), 1959–1979. https://doi.org/10.1590/0001-3765201520130385.

Ordóñez-Calderón, J.C., Gelcich, S., Fiaz, F., 2017. Lithogeochemistry and chemostratigraphy of the Rosemont Cu-Mo-Ag skarn deposit, SE Tucson Arizona: A simplicial geometry approach. J. Geochem. Explor. 180, 35–51. https://doi.org/10.1016/j.gexplo.2017.06.005.

Palarea-Albaladejo, J., Martín-Fernández, J.A., Buccianti, A., 2014. Compositional methods for estimating elemental concentrations below the limit of detection in practice using R. J. Geochem. Explor. 141, 71–77. https://doi.org/10.1016/j.gexplo.2013.09.003.

Pereira, B., Vandeuren, A., Govaerts, B.B., Sonnet, P., 2016. Assessing dataset equivalence and leveling data in geochemical mapping. J. Geochem. Explor. 168, 36–48. https://doi.org/10.1016/j.gexplo.2016.05.012.

Rivera, C., Rodrlguez, R., Pimentel, S., 2011. Horwitz Equation as Quality Benchmark in ISO/IEC 17025 Testing Laboratory. IIE Annual Conference In, 1–7.

Romary, T., Ors, F., Rivoirard, J., Deraisme, J., 2015. Unsupervised classification of multivariate geostatistical data: Two algorithms. Comput. Geosci. 85, 96–103. https://doi.org/10.1016/j.cageo.2015.05.019.

Spaggiari, C.V., Kirkland, C.L., Pawley, M.J., Smithies, R.H., Wingate, M.T.D., Doyle, M.G., Blenkinsop, T.G., Clark, C., Oorschot, C.W., Fox, L.J., Savage, J., 2011. The geology of the east Albany-Fraser Orogen - A field guide. Geological Survey of Western Australia.

van Duijvenbode, J.R., Buxton, M.W.N., Soleymani Shishvan, M., 2020. Performance Improvements during Mineral Processing Using Material Fingerprints Derived from Machine Learning—A Conceptual Framework. Minerals 10 (4). https://doi.org/10.3390/min10040366.

Wibberley, C., 1999. Are feldspar-to-mica reactions necessarily reaction-softening processes in fault zones? J. Struct. Geol. 21 (8–9), 1219–1227. https://doi.org/10.1016/s0191-8141(99)00019-x.

Wierzchoń, S.T., Kłopotek, M.A., 2018. Modern Algorithms of Cluster Analysis. Springer.

Wikedzi, A., Arinanda, M.A., Leißner, T., Peuker, U.A., Mütze, T., 2018. Breakage and liberation characteristics of low grade sulphide gold ore blends. Miner. Eng. 115, 33–40. https://doi.org/10.1016/j.mineng.2017.10.009.

Zhou, S., Zhou, K., Wang, J., Yang, G., Wang, S., 2017. Application of cluster analysis to geochemical compositional data for identifying ore-related geochemical anomalies. Front. Earth Sci. 12 (3), 491–505. https://doi.org/10.1007/s11707-017-0682-8.